Loss of the mitochondrial citrate carrier, *Slc25a1/CIC* disrupts embryogenesis *via* 2-Hydroxyglutarate

Anna Kasprzyk-Pawelec[1], Mingjun Tan[1,*], Yu Leng Phua[2,3,*], Raneen Rahhal[1], Alec McIntosh[1], Harvey Fernandez[4], Rami Mosaoa[1,5], Michael Girgis[6], Amrita Cheema[1], Lei Jiang[7], Lawrence F. Kroemer[1,4], Anastas Popratiloff[8], Cheryl Clarkson[8], Brian M. Kirmsa[9], Gray W. Pearson[1], Eric Glasgow[1], Christopher Albanese[1], Jerry Vockley[2,3 #] and Maria Laura Avantaggiati[1, #]

[1] Georgetown University Medical Center, Lombardi Comprehensive Cancer Center, Washington, D.C., USA

[2] Department of Pediatrics, Division of Genetic and Genomic Medicine, UPMC Children's Hospital of Pittsburgh, Pittsburgh, PA, USA

[3] Department of Pathology, Clinical Biochemical Genetics Laboratory, UPMC Children's Hospital of Pittsburgh, Pittsburgh, PA, USA

[4] Department of Neuroscience, Georgetown University Medical Center, Washington D.C., USA

[5] Department of Biochemistry, Faculty of Science, King Abdulaziz University, Jeddah, Saudi Arabia

[6] Department of Bioengineering Volgenau School of Engineering, George Mason University, Manassas, VA, USA

[7] Department of Molecular and Cellular Endocrinology, Arthur Riggs Diabetes and Metabolism Research Institute, City of Hope Medical Center, Comprehensive Cancer Center, City of Hope Medical Center, Duarte, CA, USA

[8] GW Nanofabrication and Imaging Center, The George Washington University, Washington, D.C., USA

[9] Department of Pediatrics, University of Mississippi Medical Center, Jackson, MS, USA

***** Denotes equal contribution

Correspondence:

Maria Laura Avantaggiati: ma364@georgetown.edu

Lombardi Comprehensive Cancer Center

Georgetown University Medical Center

NRB Rm. W315/W307/W305

Phone: +1 (202) 687-9199

E-mail: ma364@georgetown.edu

Jerry Vockley

Department of Pediatrics, Division of Genetic and Genomic Medicine

University of Pittsburgh School of Medicine and UPMC Children's Hospital of Pittsburgh 4401 Penn Avenue

Pittsburgh, PA 15224, USA

Phone: +1 (412) 692-7746

E-mail: vockleyg@upmc.edu

ABSTRACT

Biallelic germline mutations in the *SLC25A1* gene lead to combined D/L-2-hydroxyglutaric aciduria (D/L-2HGA), a fatal systemic disease uniquely characterized by the accumulation of both enantiomers of 2-hydroxyglutaric acid (2HG). How SLC25A1 deficiency contributes to D/L-2HGA and the role played by 2HG is unclear and no therapy exists. Both enantiomers act as oncometabolites, but their activities in normal tissues remain understudied. Here we show that mice lacking both *SLC25A1* alleles exhibit developmental abnormalities that mirror human D/L-2HGA. SLC25A1 deficient cells undergo premature senescence, suggesting that loss of proliferative capacity underlies the pathogenesis of D/L-2HGA. Remarkably, D- and L-2HG directly induce senescence and treatment of zebrafish embryos with the combination of D- and L-2HG phenocopies SLC25A1 loss, leading to developmental abnormalities in an additive fashion relative to either enantiomer alone. Metabolic analyses further demonstrate that cells with dysfunctional SLC25A1 undergo mitochondrial respiratory deficit and remodeling of the metabolism and we propose several strategies to correct these defects. These results reveal for the first time pathogenic and growth suppressive activities of 2HG in the context of SLC25A1 deficiency and suggest that targeting the 2HG pathway may be beneficial for the treatment of D/L-2HGA .

INTRODUCTION

The solute carrier family member SLC25A1, also known as CTP/CIC, belongs to a family of nuclear encoded ion transporters localized in the inner mitochondrial membrane where it bidirectionally transports citrate/isocitrate across the mitochondria in exchange for phosphoenolpyruvate or malate (Figure 1A) [1-3]. In the mitochondria citrate is used as an intermediate for the TCA cycle, whereas in the cytoplasm is the main precursor for fatty acid synthesis. The human *SLC25A1* gene maps to chromosome 22q11.2. Heterozygous microdeletions of this region give raise to Velocardiofacial (VCFS) and DiGeorge (DGS) syndromes [4, 5], a group of developmental disorders associated with loss of 30 to 40 genes in addition to *SLC25A1, as* well as to congenital myasthenic syndromes. Patients with 22q11.2 deletion syndrome present to the clinic with heart malformations, cleft palate, immune deficiency due to thymic aplasia, short stature and abnormal facial features, particularly microcephaly, malposition of the ears, small eyes, underdeveloped chin and flat midface. We and others have previously shown that the knock-down of the *Slc25a1a homologous* gene in zebrafish embryos induces craniofacial and heart abnormalities, suggesting a role for SLC25A1 in the pathogenesis of 22q11.2 deletion syndromes [6, 7].

Various *SLC25A1* gene mutations have also been reported in a group of developmental disorders characterized by D/L-hydroxyglutaric aciduria (D/L-2HGA), a disease hallmarked by the accumulation of the two enantiomeric forms of 2-hydroxyglutarate (2HG), D- and L [7-13]. The clinical spectrum of manifestations associated with *SLC25A1* gene mutations in D/L-2HGA is very severe, consisting of a variety of craniofacial abnormalities observed at variable frequencies, including dysmorphic features, forehead–frontal bossing, down-slanting of the eyes, flat nasal bridge, ear abnormalities, micrognathia or retrognathia, flat nose and microcephaly or macrocephaly [11]. In addition, these patients present with developmental delay and severe brain abnormalities, (cerebral atrophy, agenesis of the corpus callosum), and with hydrocephalus, respiratory insufficiency, hypotonia, epilepsy and encephalopathy. Cardiomyopathy has been described at least in one patient in D/L-2HGA [13]. Unlike in VCFS/DGS, where only one allele of the *SLC25A1* gene is lost, these mutations are found as either homozygous or compound heterozygous. We and others have previously

reported that the most severe cases of D/L-2HGA are sustained by the compound heterozygous alleles, p.Ala9Profs*82 and p.Pro45Leu (onset at 1 day, death at 1 month) [8, 11]. The p.Ala9Profs*82 mutation results in a truncated protein, while Pro45Leu maps to the region involved in mitochondrial translocation, resulting in loss of SLC25A1 mitochondrial activities. Other “hot spot” mutations that impair citrate transport activity partially or entirely, are Ser193Trp (31% residual activity), Arg282Gly/Cys (5-7%), Glu144Gln (1%) and Cys262Arg (48%). With few exceptions, for all these mutations there is a strong correlation between the extent of loss of citrate export activity and the severity of the clinical manifestations [2, 11].

It is currently unknown whether 2HG plays a direct role in the pathogenesis of SLC25A1-associated diseases. Both enantiomers are derived from the reduction of 2-oxoglutarate (α-ketoglutarate, αKG) and there are different pathways for 2HG production and elimination, in the mitochondrion or in the cytosol [14-16]. Individual forms of L- or D-2HGA are caused by mutations in the 2-hydroxyglutarate dehydrogenases L- (*L2HGDH*), or D- (*D2HGDH*) that eliminate each enantiomer by oxidation to αKG. Mutant forms of Isocitrate Dehydrogenase 1 or 2 (IDH1/2) convert αKG to D-2HG, and *IDH2* mutations can also cause D-2HGA (D-2HGA), leading to clinical manifestations more severe compared to D-2HGA caused by mutations of *D2HGDH* [13]. The promiscuous activities of physiological enzymes, including malate or lactate dehydrogenase-A lead to the production of L-2HG but alterations of these enzymes have not yet been reported in 2HGA [14]. It was initially noted that while combined D/L-2HGA is clinically more severe, the levels of D-2HG and L-2HG in these patients are moderately elevated in the urine, and very slightly in the cerebral fluids [13], compared to other forms of 2HGA and this was considered a distinct feature of D/L-2HGA. Furthermore, distinct biochemical alterations separate D/L-2HGA sustained by SLC25A1 deficiency from other forms of 2HGA, particularly the presence of increased lactate and TCA cycle intermediates in the urine, as well as respiratory complex chain dysfunction [10, 17]. Indeed, we have documented that genetic or pharmacologic inhibition of SLC25A1 impairs mitochondrial oxidative phosphorylation (OXPHOS) and rewires the metabolism towards glycolysis, essentially driving a Warburg effect [6, 18]. Mechanistically, D/L-2HG are thought to be neurotoxic and cause neuronal dysfunction [19, 20], however their activities remain understudied in normal tissues, while they have been extensively characterized in the context of tumors harboring genetic mutations of *IDH1/2* [14-17, 21-23].

These gain of function proteins produce extraordinarily high (10-30mM) amounts of 2HG. In tumors, both enantiomers act as “oncometabolites”, promoting proliferation, in large part due to their ability to out-compete αKG for binding to αKG-dependent enzymes, leading to reprogramming of the epigenome.

In keeping with the activity of SLC25A1 in the transport of citrate, the current model envisions that a deficit in the cytosolic citrate pool hampers *de novo* lipid synthesis (DNL). Indeed, the only therapy that has been so far attempted in D/L-2HGA patients consists of oral administration of citrate, but the prognosis of D/L-2HGA remains poor [11]. In this work we show that mice lacking both *Slc25a1* alleles exhibit several phenotypic characteristics typical of VCFS and DGS as well as of D/L-2HGA. In spite of the modest enrichment of D- and L-2HG in this animal model, SLC25A1 deficient mice display molecular and phenotypic characteristic that starkly overlap with those seen in mice harboring mutant forms of IDH1 or IDH2. Mechanistically, we demonstrate that similarly to inactivation of SLC25A1, 2HG induces mitochondrial dysfunction associated senescence *in vitro*, and leads to senescence and phenotypic abnormalities typical of D/L-2HGA in the model organism zebrafish. Moreover, in contrast with the prevalent mechanistic view of this disease, *Slc25a1*$^{-/-}$ mice and cells derived from patients affected by D/L-2HGA display enrichment of different lipid species but undergo prominent remodeling towards the glutamine metabolism with glutamine providing the source of 2HG. We then explored the clinical potential of phenylbutyrate, an FDA approved drug that lowers the blood glutamine levels, and we provide strong evidence for the potential clinical utility of this approach.

RESULTS

Identification of two patients with combined D/L-2-hydroxyglutaric aciduria. A female patient (Patient 897) was identified at the University of Mississippi Medical Center and presented with generalized seizures at 3 days of age. Brain MRI showed moderate to severe supratentorial ventriculomegaly with irregular margins of the lateral ventricles. The corpus callosum was markedly thinned and there was a large defect in the septum pellucidum (Figure 1B). A diagnosis of D/L-2HGA was made based on clinical urine organic acid analysis. Molecular diagnostic testing in a CLIA certified laboratory revealed two *SLC25A1* mutations in *trans*: c.844C>T (p.Arg282Cys) and a splicing mutation at position c.821+1G>A. Both these mutations have been characterized: the p.Arg282Cys mutations retain less than <5% citrate transport activity and the c.821+1G>A leads to loss of 15% citrate transport activity [11]. The patient's initial NICU admission lasted 203 days and left her ventilator dependent. Subsequently, she had multiple hospital admissions over the first 18 months of life, mostly for viral respiratory infections.

A second 3-month-old male infant (Patient 893) first presented at UPMC Children's Hospital of Pittsburgh (CHP) with a chief concern for hypotonia, apnea and feeding issues starting at 7 weeks of age. Progressively, the patient developed developmental delay, seizures, swallowing dysfunction and aspiration. Clinical urine organics acid assessment identified 2-hydroxyglutaric acid which persisted in follow-up samples. Whole exome testing identified an homozygous NM_005984.5(*SLC25A1*):c.784T>C (p.Cys262Arg), a previously described variant that retains 48% residual citrate export activity [2, 11]. During the course our studies, patient 893 was prescribed citrate supplementation by another care provider and this led to dramatic worsening of clinical symptoms and consequent hospital admission. Clinical urine organic acid analysis revealed a significant increase in excretion of 2-hydroxyglutarate which was reduced upon discontinuation of citrate therapy (not shown), suggesting that citrate therapy was detrimental for this patient. Dermal punch biopsies were performed from control donors and on both patients to establish fibroblast cultures for subsequent metabolic and molecular studies. Immunoblot analysis of these patient-derived cells revealed the presence of SLC25A1 protein (Figure 1C).

Loss of the SLC25A1 gene during embryogenesis disrupts multiple organs development. To understand the role of SLC25A1 during embryonic development we began by studying the pattern of expression of SLC25A1 protein in normal embryonic tissues. The analysis of different organs of *Slc25a1* wild-type mouse embryos at 19.5 days post-fertilization (dpf) with immunoblot showed strong expression in the brain, heart, lung, liver, colon spleen and pancreas (Figure 1D). This finding was confirmed with immunohistochemistry (Figure 1E) and immunofluorescence. Within the craniofacial region, SLC25A1 protein signal was particularly strong in the frontal region, in the mouth, eyes, palate and tongue, as well as in the cerebellum, all sites affected in human diseases sustained by SLC25A1 deficiency (Figure 1, F-G).

To then resolve the impact of SLC25A1 activity, we generated a knock-out mouse model. Mice harboring a heterozygous germline targeted deletion in one *Slc25a1* allele were produced by the Mutant Mouse Resource & Research Centers (MMRRC, C57BL/6-tm1a) with a targeting vector which is based upon the 'knockout-first' allele, as we have described previously [24]. In this vector, an IRES:lacZ trapping cassette and a *floxed* promoter-driven neo cassette is inserted between intron *1* and *2* of the *Slc25a1* gene on chromosome 16. We first expanded a population of heterozygous *Slc25a1*$^{+/-}$ mice, and intercrosses of these animals subsequently allowed studying the population of homozygous mutants (e.g., Figure 2A). Relative to wild-type and *Slc25a1*$^{+/-}$ animals, *Slc25a1*$^{-/-}$ null mice were detected at roughly normal Mendelian ratio (Figure 2B). Heterozygous mutants were born alive, appeared grossly normal with their longevity comparable to that of wild-type animals which can be followed up to 2 years of age. In contrast, only few *Slc25a1*$^{-/-}$ mice were born, but they succumbed immediately after birth (Figure 2C). On the other hand, *Slc25a1*$^{-/-}$ embryos could be detected at all stages of development from day 7 to day 19-21 dpf (Supplemental Figure 1). Thus, the knock-out of the *Slc25a1* gene leads to a highly penetrant perinatal lethal phenotype. It is relevant to note that this pattern of lethality is different from that seen with loss of other gene products essential for the lipogenic pathway, including ATP citrate lyase (*ACLY*) and fatty acid synthase (*FASN*) which both result in a more severe and completely lethal phenotype at implantation and at very early stages of development [25, 26]. This result suggested a unique mechanism(s) by which SLC25A1 loss leads to lethality, likely distinct from a simple defect in lipid synthesis.

The analysis of the *Slc25a1*$^{-/-}$ embryos at all stages of development revealed a substantial spectrum of alterations affecting multiple organs. The majority of them displayed small body size and anemia/pallor (Figure 2, D-G). The cranio-facial region and the brain were the most affected and 43% of embryos showed overt defects in neural tube closure, manifested by exencephaly or anencephaly. Additional malformations of the head and craniofacial region were detected in almost all embryos, as most of them showed malformation/absence of the ears, absence of one or both eyes, as well as cleft palate (Figure 2, E-G). A repository of computed tomography (CT) images available through the mouse phenotype consortium at UC Davis further aided in these analyses (Figure 2H) [27, 28]. The craniofacial region of *Slc25a1*$^{-/-}$ embryos at day E18.5 pf was severely dysmorphic often with unrecognizable anatomic features, including bulging or absent eyes, dilated turbinates, enlarged and protruding tongue (Figure 2, H-I and Supplemental Figure 2A). Other relevant alterations consist of brain and liver hemorrhage (Supplemental Figure 2B), heart alterations and bone abnormalities. These latter were significant and include lack of skull (Figure 2, E and G), pectus excavatum (Figure 2H), spinal deformities, including abnormal curvatures and thickness of the spine and increased cartilage content in the vertebral column reminiscent of enchondromatosis (Figure 2H and Supplemental Figure 2). Although we have not quantified these abnormalities, pectus excavatum, enchondromatosis and hemorrhages were previously described in mice harboring knock-in mutations of *IDH1/2* [29, 30]. Abdominal organs were also often malpositioned or extruded and several *Slc25a1*$^{-/-}$ mice displayed gastroschisis (Figure 2G^{3}). To further characterize these alterations, we performed H&E staining and scanning electron microscopy (SEM) focusing on the brain and craniofacial region, which revealed prominent disorganization in the developing neocortex of *Slc25a1*$^{-/-}$ embryos at E18 dpf, including alterations in neuronal size and in the orientation of neurons in the distinctive cortical layers (Figure 2, I-J). Alterations in mitochondrial morphology were also detected (not shown). The comparison of chondroblasts and collagen from the nose cartilage revealed morphological differences, with an increase in cytoplasmic vacuolization seen in *Slc25a1* deficient animals, and disruption in the directionality of collagen fibers in the matrix, another indication of alteration in the synthesis of connective tissue (Figure 2I). The tongues of virtually all *Slc25a1*$^{-/-}$ mice appeared abnormal in size and protruding, with thicker myocytes, altered directionality of fiber packages and increased connective tissue (Figure 2, I-J).

These results lead to two conclusions. First, systemic loss of SLC25A1 activity during embryonic development not only phenocopies, but also severely expands the spectrum of alterations seen in human DGS/VCFS and in D/L-2HGA, making it likely that the complete ablation of the *human SLC25A1* gene would lead to death in utero. Second, the data provocatively demonstrate the existence of some overlap between the phenotype of SLC25A1 homozygous mutant mice and mice harboring mutations of either IDH1/2, particularly as it pertains to the brain, heart, collagen and bone abnormalities [29-32], a point that is further explored below.

Loss of SLC25A1 leads to remodeling towards lipid and glutamine metabolism. The current model envisions that the pathogenesis of diseases due to impaired SLC25A1 activity is sustained by the deficit of citrate export from the mitochondria to the cytoplasm, which results on one side in impairment of DNL, and on the other to mitochondrial accumulation of αKG and consequent production of 2HG. We began testing this model by performing targeted and untargeted metabolomic and lipidomic analyses, paralleled by immuno-blot experiments interrogating the main pathways involved in lipid biosynthesis and we also assessed the concentration of citrate and 2HG. To our surprise, the levels of key lipogenic enzymes, fatty acid synthase (FASN) and acetyl-CoA carboxylase Alpha (ACC1) were up-regulated in the brain and MEFs derived from *Slc25a1*$^{-/-}$ mice, at both protein and mRNA level (Figure 3, A-C). Pathway enrichment analysis unequivocally showed enhanced triglyceride species in *Slc25a1*$^{-/-}$ brains (Figure 3D), as well as of phospholipids and ceramides (not shown). The analysis of the amniotic fluids (AF), which contain the urine and by-products of the whole embryo metabolism, confirmed the enrichment of many lipid species including linoleic acid, phospholipids, glycerolipids, sphingolipids, arachidonic, steroid, and bile acid biosynthetic pathway, along with the previously reported increase in the Warburg effect (Figure 3, E), [6, 18]. The metabolic profile of the patient-derived fibroblasts was surprisingly similar to that seen in *Slc25a1*$^{-/-}$ mice, (considering the different tissue of origin) and showed an enrichment of lipid species (Figure 3, F-G). Importantly, the concentration of citrate was moderately elevated in the patient-derived fibroblasts and in the AF of *Slc25a1*$^{-/-}$ mice, but itaconate, which is derived from cytosolic citrate *via* the activity of *IRG1*, was significantly increased (Figure 3, H-I), suggesting an abundance of cytosolic citrate. Finally, the analysis of the TCA cycle intermediates in the AF revealed higher excretion of all metabolites, but particularly of αKG and succinate, consistent with the

alterations reported in the urine of individuals affected by human D/L-2HGA (Figure 3I) [8, 9, 11]. These results indicate that SLC25A1 is not rate limiting for maintenance of the lipid pool during embryonic development, at least in the animal and cellular systems that we have analyzed, and are consistent with the documented existence of pathways able to replenish cytosolic citrate in cells lacking SLC25A1, including *via* glutamine reductive carboxylation by IDH1 [33, 34]. Indeed, the expression levels of IDH1 and of glutaminase 1 (GLS1) were elevated in the brain and cells derived from *Slc25a1* deficient mice (Figure 3, A-C). Untargeted metabolomic analysis demonstrated enrichment of glutamine and glutamate metabolism, of the urea cycle and ammonia metabolism, indicative of ammonia release due to the conversion of glutamine to glutamate *via* the action of GLS1 (Figure 3J).

SLC251A deficiency results in modest L/D-2HG enrichment but phenocopies the transcriptome of IDH1/2 mutations. It was noted before that in combined D/L-2HGA the levels of D-2HG and L-2HG were moderately elevated in the urine, and very slightly in the cerebral fluids, compared to other forms of individual L- or D-2HGA [13]. According to this, using different embryos derived from different litters and two different methods for 2HG detection (LC/MS/MS and GC/MS/MS), the total pool of 2-HG was moderately elevated in the P893 and P897 fibroblasts (Figure 3H, 1.1 Log2 FC) and in the amniotic fluids of *Slc25a1* deficient mice (less than 2-fold), but was significantly higher in the brains reaching a five-fold average enrichment compared to control (Figure 4, A-B). To determine the relative enrichment of the D- and L- enantiomer, a chiral derivatization method was employed [35] (see Supplemental Figure 3A for the L/D peak separation). We established that the D-enantiomer accounts for approximately 70% of the total pool and represents the main pool enriched in *Slc25a1*$^{-/-}$ mice relative to control (Figure 4, C-D). A similar ratio was also seen in the patient-derived fibroblasts, where most of the 2HG was detected in the media (not shown). Importantly, the acute knock-down of *SLC25A1* in cells harboring wild-type *IDH1/2* genes led to a similar extent of enrichment of D-2HG indicating that SLC25A1 depletion directly causes D-2HG accumulation (Figure 4E). Since the concentration of 2HG is known to fluctuate even in the same individual(s), to validate these results, we analyzed previously published data derived from nine patients affected by D/L-2HGA [8, 11] and found a similar, but not exclusive, prevalence of D-2HG (Figure 4F).

To gather a deeper understanding of the pathways altered in SLC25A1-dependent manner we next performed RNA sequencing experiments in the brain of wild-type and *Slc25a1*$^{-/-}$ mice. Three mice per group, each from a different litter and at similar stage of development (E18.5 dpf), were used. This analysis detected 1395 genes uniquely regulated in *Slc25a1* homozygous mutants (Figure 4G). Hierarchical clustering of significantly altered genes revealed a good separation of the transcriptome of wild-type and *Slc25a1*$^{-/-}$ mice, with the majority of differentially regulated genes being up-regulated, while only a small sub-set was down-regulated (Figure 4H). Reactome pathway enrichment analysis identified the gene sets over-represented in *Slc25a1*$^{-/-}$ mice (Figure 4I), which included genes involved in Immune Cytokine Signaling, Signaling by NRTKs, AP1 Transcription & MAPK Signaling, Cellular Senescence, Carbohydrate Metabolism, Complement Activation, Innate Immune System Function, Collagen Metabolism, Endoplasmic Reticulum Response, Hyaluronan Metabolism & Processing, Semaphorin Signaling, Coagulation & Platelet Activation, as well as, notably, Hypoxia Response and VGF. These findings were surprising, as it was immediately obvious that numerous pathways enriched in *Slc25a1*$^{-/-}$ brains exhibited commonalities with gene signatures that were previously seen in mice harboring oncogenic *Idh1* or *Idh2* mutations, and particularly with a model of D-2HGA induced by systemic expression of IDH2^{R172H} or IDH2^{R140Q} mutants, where the extent of 2HG enrichment was however an average 200-fold relative to control [32]. We then conducted a comparative analysis between the RNAseq data obtained from *Slc25a1*$^{-/-}$ brains and GEO datasets (Gene Expression Omnibus) available for the study on IDH2^{R172H} or IDH2^{R140Q} in the heart [32], or IDH1^{R132H} in the subventricular zone [31]. This approach demonstrated that a number of signals over-represented in *Slc25a1*$^{-/-}$ mice indeed overlaps with gene signatures previously detected in these studies (Figure 4J). The highest significance of overlap was detected with the IDH2 mutant model, particularly in the Collagen Metabolism & ECM Organization, in some components of the Immune Cytokine Signaling, Signaling by NRTKs, Semaphorin Signaling, Coagulation & Platelet Activation and Hypoxia Response and VGF.

We conclude that loss of SLC25A1 activity leads to reprogramming of the transcriptome in a manner similar to that seen with IDH1/2 mutations, hinting at the full pathogenic potential of 2HG even at modest levels of enrichment.

2HG leads to mitochondrial dysfunction and senescence, recapitulating the effects of SLC25A1 loss. The RNAseq data suggested that senescence is induced by loss of SLC25A1 (Figure 4I) and senescence is known to drive neuro-developmental and neural tube closure defects [36-38]. Senescence occurs physiologically in small discrete areas of the developing mouse embryo, however it is only detectable during a specific time window, initiating on day E11 and disappearing by E17.5 [35]. Unlike developmental senescence that requires the activity of p21, premature senescence leads to induction of both p53 and p21, of histone gammaH2AX, as well as of the mammalian Target Of Rapamycin, mTOR [39-42]. In conditions typically used for tissue culture, primary cells and MEFs survive for 8-11 populations before undergoing premature senescence. We found that both the *Slc25a1*$^{-/-}$ MEFs cells and the patient-derived fibroblasts exhibited a proliferation defect at very early passages (between 2 and 5), highly suggestive of senescence (Figure 5A and not shown). Accordingly, these cells displayed enhanced senescence-associated beta-galactosidase *(*SA-β-GAL) activity, and increased levels of p53, p21, and of mTOR (Figure 5, B-G). This was accompanied by stark over-expression of the Senescence Associated Secretory factors, SASPs, including interleukins (IL-6, IL-10, IL-1β), tumor necrosis factor-α (TNFα) and of AMP kinase, which together with IL-10 and p53 is a marker of mitochondrial dysfunction associated senescence [43] (Figure 5H). More importantly, the freshly isolated brains of *Slc25a1*$^{-/-}$ mice at day 19 dpf displayed enrichment of senescence markers at both protein and mRNA levels and reacted with antibodies directed against p21 in the area of exencephaly (Figure 5, I-K). To rule out that senescence is the artificial result of passaging cells in culture or a reflection of developmental delay in SLC25A1 deficient mice, we assessed the effects of the acute knock-down of *SLC25A1 vi*a RNA interference. Loss of SLC25A1 leads to a relatively rapid (within one week) induction of senescence (Supplementary Figure 3B).

Given that mitochondrial dysfunction is a driver of senescence, we next studied the respiratory capacity of cells lacking functional SLC25A1. Consistent with our previous work [6, 18], both *Slc25a1*$^{-/-}$ MEFs and the patient fibroblasts exhibited a very significant deficit in the basal, maximal and spare respiratory capacity, as well as in mitochondrial ATP production (Figure 6, A-B). Several previous studies have shown that 2HG can either inhibit or induce mitochondrial respiratory capacity in tumor cells of different origin [44, 45]. To determine whether D- or L-2HG alone or in combination can mimic SLC25A1 deficiency in normal tissues, we used primary human

fibroblasts. The results of these experiments were striking. Both D- and L- significantly blunted respiratory activity and this inhibitory effect was enhanced when they were mixed together (Figure 6, C-D). Furthermore, treatment with low concentrations of either enantiomer over the course of 5 days led to strong induction of SA-β-GAL activity which did not increase when the concentration was titrated up to 1- to-10 mM, reflective of tumor concentrations (Figure 6, E-H), thus suggesting that induction of senescence is a mechanism by which normal cells respond to low levels of 2HG. D- and L-2HG, individually, also induced p53 and of p21, however this effect was only relatively dose-dependent, but it was enhanced by the combination (Figure 6, I and J).

Thus, loss of SLC25A1 activity diminishes the proliferative capacity of normal cells leading to the induction of mitochondrial dysfunction associated senescence. Further, these results argue that this effect is at least in part mediated by the combination of D- and L-2HG.

Treatment of zebrafish embryos with D- and L-2HG perturbs embryonic development. The evidence that D- and L- 2HG disrupt embryonic development comes predominantly from mice harboring *Idh1/2* knock-in alleles as well as from the finding that transplanting IDH2 mutant tumors in nude mice induces cardiomyopathy, implying a direct role for tumor-produced D-2HG [31]. One plausible explanation for the severity of the phenotypes seen in *Slc25a1*$^{-/-}$ mice and in human D/L-2HGA is the unique concomitant presence of both enantiomers, a trait that separates D/L-2HGA from other forms of individual 2HGA. To directly investigate the effects of D- and L-2HG on embryonic development, we used the zebrafish model as an experimental platform, employing the cell permeable Octyl-R/D- or Octyl-S/L- 2HG. Importantly, we previously reported that the knock-down of the homologous *Slc25a1* gene leads to severe developmental defects of zebrafish embryos resulting in alterations in the brain, craniofacial region and in the heart, in part recapitulating features of DGS, VCGS and of D/L-2HGA [6]. By performing dose-response experiments, we detected relevant phenotypes at concentrations ranging between 20-100 μM of either enantiomer. The main organ affected was the brain, which was small and bulging (Figure 7, A and B). In addition, virtually all treated embryos exhibited small head, jaw and eyes, larger hearts as well as pericardial edema and these phenotypes were induced in a dose-dependent fashion (Figure 7, A-C). At an 80 μM R/D-2HG dose, all embryos exhibited evidence of facial

dysmorphism and disorganization of the brain tissue (Figure 7B). In addition, an increased SA-β-GAL signal was detected in the brain, in the yolk, around eyes, and in the tail (Figure 7, D-E). Both the R/D and S/L-2HG also induced a cardiovascular phenotype consisting of heart enlargement and reduced ability of the heart to pump blood (Figure 7C and Supplemental Video 1), highly indicative of cardiomyopathy, which likely caused impaired blood flow through the body and tail (Supplemental Videos 2 and 3). Alterations in the vertebral column and in the body curvature were also very significant, and are in part consistent with the phenotype of *Slc25a1*$^{-/-}$ mice (Figure 7, A and G). This spectrum of phenotypic alterations is highly similar to that previously seen in zebrafish and mice lacking *Slc25a1*. However, we also identified distinctive traits specific to D- and L-2HG treatments in zebrafish, currently of unclear significance, the most notable of which is the development of lymphatic cysts, a characteristic associated with the knockout of the *wnt5a* gene [46] (not shown). In order to understand whether the combination of these enantiomers leads to enhanced pathological features, we performed mixing experiments combining D- and L-2HG at different ratios mimicking the ratio seen in D/L-2HGA with a prevalent enrichment of D-2HG (see Figure 4, A-F). This approach yielded a distinct additive effect, resulting in the amplification of abnormalities that became prominent even at lower concentrations. Specifically, low concentrations of S/L-2HG alone, similarly to R/D-2HG, induced a mild phenotype, which however became severe at higher doses (Figure 7 F). Combining R/D- and S/L at doses at which neither enantiomer alone induced severe alterations, significantly worsened the phenotype (Figure 7G, panel 1). Strikingly, this effect was seen not only when the R/D-2HG was prevalent, but also when the relative abundance was inverted with a prevalence of the S/L-2HG (Figure 7G, compare panel 2 and 3).

In conjunction with our previous findings, these data offer compelling evidence that D/L-2HGA sustained by SLC25A1 deficiency relies at least in part on the combination of D- and L-2HG.

Targeting the glutamine metabolism with phenylbutyrate lowers the 2HG levels in human models of D/L-2HGA. There are no effective treatments for combined D/L-2HGA. While reduced cytosolic citrate has been previously postulated as a major pathological driver of this disease [47], interventional use of citrate remains controversial [10] and, as shown here, lipids are not limiting in SLC25A1 deficient cells or in patient-derived. In addition,

patient 893 was prescribed citrate supplementation, leading to a worsening of clinical symptoms, which resolved when the therapy was interrupted. Indeed, we found that citrate supplementation significantly impaired oxygen consumption and mitochondrial respiration in P893 cells and manipulation of the extra-cellular citrate levels can also trigger cell death and senescence, as shown by other groups and confirmed in our experiments (Supplemental Figure 4, A-C). On the other hand, our data have demonstrated direct pathogenic effects of D-2HG, thereby establishing a strong rationale for targeting this metabolic alteration. Given the lack of clinically available drugs able to lower 2HG levels, we focused on the up-stream metabolic pathways leading to 2HG production. Specifically, our results revealed that patient derived fibroblasts and tissues lacking a functional SLC25A1 protein have enhanced glutamine-, glutamate-, urea and ammonia-related pathways, and glutamine is known to be source of D-2HG production [48, 49]. Indeed, a tracing experiment performed with [U-^{13}C]glutamine showed that the 2HG pool in *Slc25a1*$^{-/-}$ MEFs comes from glutamine (Supplemental Figure 4D). On this basis, we hypothesized that blocking the glutamine pathway could improve at least some of the clinical manifestations due to SLC25A1 deficiency offering a strategy for lowering the levels of 2HG in patients. There are several compounds that act by depleting glutamine with different mechanisms, some of which are FDA approved. We decided to explore the effects of phenylbutyrate (PB) which is standard of care for the management of urea cycle disorders [e.g.,50, 51]. Pharmacokinetically, phenylbutyrate undergoes one cycle of β-oxidation to form phenylacetyl-CoA, which subsequently conjugates to glutamine to form phenylacetylglutamine (PAG) through the enzyme phenylacetyl-CoA:L-glutamine-N-acetyltransferase, and is eventually excreted from the kidney (Figure 8A). Therefore, PB acts as a glutamine sink. No toxicity has been observed at dose regimens of 5 to 20 grams daily given in three equally divided doses. At 18 months of age, patient 897 had prolonged and repeated hospitalizations due to respiratory failure that left her ventilator dependent. Under an IRB protocol, patient 897 was treated with sodium phenylbutyrate at 250 mg/kg/day in 4 divided doses. Within 4 days, the patient was weaned off her ventilator settings and was soon discharged. After several months on treatment, this patient displayed additional improvement in the awareness of surroundings, ability to make eye contact and social skills (Figure 8B). While completely ventilator dependent at presentation and diagnosis, P897 now tolerates up to 4 hours at a time off the ventilator and episodes of respiratory distress requiring additional manual bagging have been eliminated. This patient has had several

viral infections (including COVID-19) since starting sodium phenylbutyrate, none of which have required hospitalization. Patient 893 only recently started treatment with Ravicti (glycerol phenylbutyrate) and has not had a clinical response. However, the urine excretion of 2HG was reported to be undetectable through clinical urine organic analysis (UPMC Children's Hospital of Pittsburg Clinical Biochemical Genetics Laboratory).

In order to confirm the effectiveness of PB at a cellular level, we performed an untargeted metabolomic analysis on the patient-derived fibroblasts to assess the changes in intracellular metabolites induced by PB treatment and we compared it with the metabolomic analysis performed at baseline. First, global analysis of the patient-derived fibroblasts metabolomics' data was performed using hierarchal distance clustering based on Euclidean distance metric which revealed two distinct clusters, the largest cluster consisting of controls and phenylbutyrate-treated patient fibroblasts, and the second representing the untreated patient fibroblasts (Figure 8C). This result argues that PB reverts the metabolic profile of the patient fibroblasts. We next conducted a pathway enrichment analysis by focusing specifically on the examination of metabolites down-regulated in PB treated cells and we compared them to those previously found up-regulated at baseline (Figure 3F). Strikingly, PB treatment resulted in highly significant reduction in αKG (60%), of 2HG (20%) as well as of citrate (80%) (Figure 8, D-E). Moreover, it induced the *de novo* formation of PAG, leading to an enrichment of >16,000 fold and thus confirming the presence of the active biochemical reaction between glutamine and phenylacetyl-CoA. In addition, PB induced a reversion of virtually all metabolic pathways previously found up-regulated in untreated cells (Figure 8F, indicated in blue and compare with Figure 3, F-G).

These data support the proposition that PB can be effective in some patients affected by D/L-2HGA and could be clinically attempted when there is enough information on the global metabolic profile. We were able to gather important clues by analyzing small amounts of amniotic fluids in mice, and given the high sensitivity of most metabolomic techniques, it should be possible to perform similar analyses on repeated collections of the urine or even of small amount of blood from these patients, an approach that may be pivotal in guiding clinical decisions.

DISCUSSION

Using a multifaceted approach that includes a novel murine model of D/L-2HGA we have demonstrated that the phenotypic alterations due to loss of SLC25A1 recapitulate and expand those seen in known human developmental disorders. We have previously shown that the knock-down of the *slc25a1* gene in *zebrafish* also leads to lethality [6]. This pattern of highly penetrant lethality raises the possibility that complete loss of SLC25A1 activity is incompatible with human embryonic development and would lead to stillbirths. Thus, the clinical prevalence of this genetic alteration may be still underestimated. This work also reveals that the molecular and phenotypic alterations arising from SLC25A1 deficiency are in large part sustained by the accumulation of 2HG as demonstrated by the observation that both in tissue culture cells and in *zebrafish*, treatment with D/L-2HG was able to recapitulate many salient features sustained by SLC25A1 loss. Moreover, in both tissue culture cells and in *zebrafish*, 2HG induces senescence, a finding only in apparent contrast with its definition of as “oncometabolite”. Our data essentially suggest that the first response of normal cells to 2HG is the induction of growth arrest and senescence and that dismantling of downstream tumor suppressor pathways, including p53, is necessary for transformation, similarly to oncogene induced senescence.

The main impact of our findings is in the observation that at least in our model systems, SLC25A1 loss leads to only a modest enrichment of 2HG, just 5 folds above background in the brain, yet SLC25A1 deficient mice display the spectrum of alterations seen in *Idh1/Idh2* mutant mice. However, these mutant proteins are known to produce D2HG at extraordinarily high concentrations. On the other hand, the fact that both enantiomers could be detected in wild-type mice suggests that physiological functions for 2HG likely exist, though remain elusive. Alternatively, as proposed in the literature, D/L-2HG is produced in cells and tissues as a byproduct of the metabolism under conditions of extreme metabolic demand, requiring highly timed elimination. Recent work has revealed that L-2HG, but not D-2HG, is present at very high concentrations at the earliest steps of embryonic development in murine embryos, during the two-cells to blastocyst transition, but completely disappears in blastocysts [52]. The knockdown of *L2hgdh,* impedes epigenetic remodeling, disrupts development, leading to the collapse of blastocysts. These observations, together with the existence of two enzymes, L2HGDH and D2HGDH, which are conserved throughout evolution, suggest the existence of a

strong selective pressure for clearing 2HG during embryonic development. They also suggest that there is likely a very narrow window in which D and L-2HG can be tolerated, which helps explain why even small elevations can be deleterious, as is the case with SLC25A1 deficiency.

It is interesting to note that as of now, the only enzymes dedicated to the clearance of D and L-2HG appear to exist only in the mitochondria, perhaps implying that cytosolic accumulation, when it occurs, might be more pathogenic even at lower, but sustained concentrations. Although we have not studied the sub-cellular localization of 2HG, we did not find obvious alterations in the levels of L2HGDH and D2HGDH (not shown), suggesting different mechanisms for its accumulation. We tend to exclude that SLC25A1 deficiency leads to mutations of IDH1/2 for several reasons: first, 2HG increases at similar levels and acutely as a result of the knock-down of *SLC25A1* in cells in culture harboring wild-type IDH1/2 alleles (Figure 4E); second, *IDH1/2* mutations were not detected in the patients presented in this study. An attractive possibility is instead that the activity of wild-type IDH1 and/or IDH2 is engaged to compensate for SLC25A1 loss, and contributes to the production of the D-enantiomer, as it is now well established that these enzymes can catalyze the conversion of αKG to D-2HG [15, 53, 54]. In keeping with the glycolytic switch seen in the *Slc25a1*$^{-/-}$ brains and in the patient-derived cells, LDH-A could contribute to 2HG accumulation with the synthesis of the L-enantiomer.

This study informatively reveals the existence of similarities as well as differences between the phenotype of mice harboring *Idh1/2* mutations and SLC25A1 deficient mice. Brain and heart abnormalities as well as post-natal lethality were previously described in rodents harboring the R132H and R140Q IDH2 mutations, whose transcriptome profile displays high similarity with *Slc25a1*$^{-/-}$ deficient brains [31, 32, 55]. Furthermore, mice expressing a conditional IDH1-R132Q under the control of the collagen 2 promoter exhibit pectus excavatum, which is also present in *Slc25a1*$^{-/-}$ mice, and enchondromatosis [29]. Finally, the L2hgdh knockout in mice leads to brain abnormalities, to leukoencephalopathy, neuroinflammation and early death [56]. Yet, the phenotype of *Slc25a1*$^{-/-}$ mice is not entirely recapitulated by either the knock-down of L2HGDH or D2HDH, or by IDH1/2 knock-in models, not only for the broader spectrum of alterations affecting multiple organs, but especially for their severity. The simplest explanation for this finding is that additional SLC25A1 activities

unrelated to 2HG accumulation and perhaps to citrate export do exist and are required for normal development. Our ongoing studies in fact suggest that the phenotype of cells treated with known SLC25A1 inhibitors of the citrate binding activity or harboring the *SLC25A1* knock-down are different.

Citrate therapy has previously been reported to stabilize the severity and frequency of seizures in combined D/L-2HGA patients [11]. However, citrate treatment paradoxically increased our patient urinary excretion of TCA cycle intermediates including malate and succinate indicative of mitochondrial stress, and the patient exhibited an acute metabolic decompensation that quickly resolved upon discontinuation of citrate. This finding is in agreement with at least one previous report that treatment of patient fibroblasts with 4 mM citrate led to reduced mitochondrial respiratory capacity and citrate supplementation did not produce sustained improvement in the patient [10]. Thus, the merits of citrate therapy for this disorder remain questionable, are potentially mutation-specific and, ultimately, the clinical management of these patients will require a careful assessment of the global associated metabolic alterations, as we discussed above. Here on the other hand, we have demonstrated that treatment with PB, an FDA-approved medication for urea cycle disorders and well known to act as a glutamine and ammonia sink, significantly improved the metabolic state of patient derived fibroblasts reducing the accumulation of citrate, αKG and 2HG and led to clinical improvement. Phenylbutyrate also reverted global metabolic alterations seen in these cells before treatment indicating its potential to not only target the accumulation of toxic metabolites (e.g., 2HG) but also to induce secondary changes in the core pathways altered when SLC25A1 activity is compromised. Phenylbutyrate is well known also as a deacetylase inhibitor and belongs to the category of drug proposed to act as “differentiation therapy”. We do not exclude a beneficial effect of this drug also on reprogramming the acetylome. Alterations in acetylation have been described in cells harboring *IDH1/2* mutations [57, 58]. In the context of SLC25A1 loss they may arise as a consequence of the compensatory response that directs Ac-CoA predominantly towards the lipid synthetic pathway.

Finally, it is important to note that the spectrum of molecular and biochemical alterations seen in *Slc25a1*$^{-/-}$ mice is global and various tissues might respond and adapt to SLC25A1 loss differently. We believe that the

phenotype of *Slc25a1*$^{-/-}$ mice is complex, likely multi-factorial, mediated by SASPs, by 2HGs, by citrate and also by mTOR signaling, as well as by HIF1 signaling, that might act synergistically to perturb normal embryonic development in the most vulnerable organs. In addition, our studies reveal the existence of several low penetrance phenotypes in SLC25A1 deficient mice, which include anophthalmia, pectus excavatum and gastroschisis and not all mice exhibit defects in neural tube closure. These lower -penetrance phenotypes raise the important question of "second site modifiers" that likely impinge upon the outcome of SLC25A1 loss in a tissue or context specific manner. Though many of the pathological manifestations due to SLC25A1 deficiency are likely irreversible, as they are acquired during embryogenesis and development, we predict that this study will inform on therapeutic strategies able to ameliorate at least some aspects of these devastating disorder.

Methods.

Cell culture. The A549 cell line was obtained from ATCC or from the tissue culture core facility at LCCC. Cells were grown in Dulbecco's Modified Eagle's Medium (DMEM 4500 mg/L glucose) or RPMI-140 media supplemented with 10% fetal bovine serum, 2 or 4 mM L-glutamine, 1 mM sodium pyruvate and 1% antibiotic solution. The S*LC25A1*-specific shRNA vectors were purchased from Sigma (TRCN0000232825; TRCN0000255350) and validated before (6,18,24). Octyl-2-HG (Cayman 16366, 16367) was diluted in PBS pH 7.2.

Mice. The original S*lc25a1* tm1a strain was purchased from Mutant Mouse Resource Research Center (MMRRC) (C57BL/6N-*Slc25a1*$^{tm1a(EUCOMM)Wtsi}$, RRID:MMRRC_042258-UCD). The targeting vector allows for constitutive or conditional deletion of the *SLC25A1* gene through the incorporation of an IRES:lacZ trapping cassette which is inserted between introns 1 and 5 of the *Slc25a1* gene [24]. Mice were maintained on a 12h light/dark cycle and were supplied with food and water ad libitum. To obtain mouse lacking *Slc25a1* we crossed heterozygous *Slc25a1*$^{+/-}$ heterozygous mice. Pregnancy was confirmed by checking for vaginal plugs and the increase in body weight measured weekly.

Embryos, brains and amniotic fluids collection. Pregnant mice were euthanized at different stages of pregnancy and whole embryos were collected. Typically, embryos were harvested at E9.5-E19, and tips of tails were collected for genotyping. For IHC, embryos were fixed in 4% paraformaldehyde overnight, transferred to

80% EtOH and sent for histological processing. Paraffin embedding, sectioning and hematoxylin/eosin staining of embryos tissue sections were performed by Histology and Microscopy Core of Georgetown University or by VitroVivo Biotech. To collect the amniotic fluid, and avoid cross-contamination, we typically selected embryos distally located. After transferring the embryos to a clean dish, the amniotic fluid was collected by 1-mL syringe and 27-gauge needle. For biochemical and molecular analysis, indicated organs were dissected, quickly washed in PBS and snap frozen in liquid nitrogen. For the collection of the brains, skin and skull (when present) were carefully removed. The isolated brains were quickly washed in PBS twice, snap frozen in liquid nitrogen and stored at -80°C until processed for further analyses.

2HG quantification with LC/MS/MS and GS/MS/MS. For LC/MS a targeted metabolomics method was used to quantitate 2-HG using QTRAP® 7500 LC-MS/MS System (Sciex, MA, USA). The 2HG standard was from Sigma Aldrich (# 90790-10MG). For the purpose, 75 µL of extraction buffer (methanol/water 50/50) containing 200 ng/mL of 4-nitrobenzoic acid as internal standard for negative mode was added to the cell pellet and sample tube was plunged into dry ice for 30 sec and 37 °C water bath for 90 sec. This cycle was repeated for two more times and then samples were sonicated for 1 minute. The samples were vortexed for 1 min and kept on ice for 20 minutes followed by addition of 75 µL of ACN. The samples were incubated at -20 °C for 20 minutes for protein precipitation. The samples were centrifuged at 13,000 rpm for 20 minutes at 4 °C. The supernatant was transferred to MS vial for LC-MS analysis. 20 µL of each prepared sample was mixed to generate the pooled QC sample. For GC-TOF amniotic fluids or tissue samples were processed using 500 µL of 50% methanol in water containing the internal standard (4-Nitrobenzoic acid, prepared in MeOH at a concentration of 20 µg/mL). The samples were homogenized on ice to ensure tissue lysis and metabolite extraction was then vortexed for 2 minutes. A volume of 10 µL was withdrawn from the homogenized tissue suspension for the protein quantification assays. The samples were vortexed for 2 minutes and left for 2 hours at room temperature. The BCA kit used for the protein quantification assay was Pierce™ BCA Protein Assay Kit (Cat # 23225). A volume of 20 µL of methoxyamine (20 mg/mL) was added to the dried tissue extracts and then heated in an agitator at 60 ^{0}C for 30 minutes. This was followed by 100 µL of MSTFA. The vials were transferred to an agitator to heat at 60 ^{0}C for 30 more minutes. Finally, the vials were capped and a volume of 1.5 µL was injected directly to the GC-MS. The samples were allowed to react at room temperature for 20

minutes before being transferred to the GC for injection. Briefly after the derivatization process, a volume of 1.5 µL of the derivatized solution was injected in (1:10) split mode into an Agilent 7890B GC system (Santa Clara, CA, USA) that was coupled with a Pegasus HT TOF-MS (LECO Corporation, St. Joseph, MI, USA). Separation was achieved on a Rtx-5 w/Integra-Guard capillary column (30 m x 0.25 mm ID, 0.25 µm film thickness; Restek Corporation, Bellefonte, PA, USA), with helium as the carrier gas at a constant flow rate of 0.9 mL/min. The temperature of injection, transfer interface, and ion source were set to 150, 270, and 320 °C, respectively. The GC temperature programming was set to 0.2 minutes of isothermal heating at 70 °C, followed by 6 °C/min oven temperature ramping to 270 °C, a 7.0 minute isothermal heating of 270 °C, 20 °C/min to 320 °C, and a 2.0 min. isothermal heating of 320 °C. Electron impact ionization (70 eV) at full scan mode (40–600 *m*/*z*) was used, with an acquisition rate of 20 spectra per second in the TOF/MS setting.

Metabolomic and Lipidomics. Metabolomic (targeted and untargeted was performed as described before (18,24). The lipidomic method used in the brains of *Slc25a1*$^{-/-}$ mice, is designed to measure 19 classes of lipid molecules which includes diacylglycerols (DAG), chloesterol esters (CE), sphingomyelins (SM), phosphtatidylchloine (PC), triacylglycerols (TAG), free fatty acids (FFA), ceramides (CE), dihydroceramides (DCER), hexosylceramide (HCER), lactosylceramide (LCER), phosphatidylethanolamine (PE), lysophosphtatidylchloine (LPC), lysophosphatidylethnolamine (LPE),phosphatidic acid (PA), lysophosphatidic acid (LPA), phosphatidylinositol (PI), lysophosphotidylinositol (LPI), phosphatidylglycerol (PG) and phosphatidylserine (PS) using QTRAP® 5500 LC-MS/MS System (Sciex). For the purpose, 20 µL of each amniotic fluid sample was dissolved in 100 µL of chilled isopropanol containing internal standards (list provided in Supplementary Table 1) was added and samples were vortexed. The samples were vortexed again for 1 min and kept on ice for 30 minutes. Samples were incubated at -20 °C for 2 hours for complete protein precipitation. The samples were centrifuged at 13,000 rpm for 20 minutes at 4 °C. The supernatant was transferred to MS vial for LC-MS analysis. Five µL of each sample was injected onto a Xbridge amide 3.5 µm, 4.6 X 100 mm (waters) using SIL-30 AC auto sampler (Shimazdu) connected with a high flow LC-30AD solvent delivery unit (Shimazdu) and CBM-20A communication bus module (Shimazdu) online with QTRAP 5500 (Sciex, MA, USA) operating in positive and negative ion mode. Obtained results were analyzed using MetaboAnalyst.

Brain TCA cycle analyses. Tissue samples were mixed with 400 µL of MeOH containing the internal standard (4-Nitrobenzoic acid) which was prepared in MeOH at a concentration of 30 µg/mL and homogenized for 60 seconds. A volume of 10 µL was withdrawn from the tissue suspension for the protein concentration assay. The samples were mixed for 2 minutes, left at -20 °C. for 2 hours then centrifuged for 30 min at a speed of 16,000 X g and a temperature of 4 °C. The supernatant was separated and transferred to the GC vials then dried under vacuum at room temperature. Samples were derivatized and injected into GCMS instrument. Protein concentration was determined using BCA assay. The Briefly after the derivatization process, a volume of 2.0 µL of the derivatized solution was injected in a splitless mode into an Agilent 7890B GC system (Santa Clara, CA, USA) that was coupled with a Pegasus HT TOF-MS (LECO Corporation, St. Joseph, MI, USA). Separation was achieved on a Rtx-5 w/Integra-Guard capillary column (30 m x 0.25 mm ID, 0.25 µm film thickness; Restek Corporation, Bellefonte, PA, USA), with helium as the carrier gas at a constant flow rate of 0.8 mL/min. The temperature of injection, transfer interface, and ion source was set to 150, 270, and 320 °C, respectively. The GC temperature programming was set to 0.2 min. of isothermal heating at 70 °C, followed by 6 °C/min oven temperature ramping to 300 °C, a 1.0 min. isothermal heating of 300 °C, 20 ° C/min to 320 °C, and a 2.0 min. isothermal heating of 320 °C. Electron impact ionization (70 eV) at full scan mode (40–600 m/z) was used, with an acquisition rate of 20 spectra per second in the TOF/MS setting.

Genotyping. Mouse tail biopsies and agarose gel electrophoresis was used for analysis of PCR products. The PCR conditions used were as follows: 94 °C for 1 minute, 5 cycles at 94 °C for 30 s, 63 °C for 40s, 68 °C for 1 min; followed by 30 cycles (94 °C for 30 seconds, 55 °C for 40 seconds, and 72 °C for 1 min), 72 °C for 7 min then kept in 4 °C before use. The primers used for genotyping are indicated in Table S1.

Mouse embryonic fibroblasts isolation. Freshly dissected embryos at E10-E14 were used for isolation of mouse embryonic fibroblasts (MEFs). Brain, liver, internal organs and tail were removed, and the remaining tissues were rinsed with PBS and transferred to a 10 cm plate. Embryos were then minced with a sterile razor blade in the presence of TrypLE™ Express Enzyme (Gibco™, 12604021) following by 10 min incubation on a shaker at RT. Finally, the cells were pipetted multiple times to further disintegrate the tissue, and then the freshly isolated cell were cultured in high glucose DMEM medium (Dulbecco's Modified Eagle Medium with 10% fetal bovine serum, 4500 mg/L glucose, 4 mM L-glutamine, 1 mM sodium pyruvate and 1% antibiotic solution).

Protein analysis and immunoblot. Proteins from cells or frozen tissue samples, grinded in liquid nitrogen, were homogenized in RIPA buffer supplemented with cOmplete Mini Protease Inhibitor Tablets (Roche, 11836153001). Protein quantification was done by using Coomassie (Bradford) Protein Assay Kit (Pierce). Equal amount of protein lysate was loaded and separated in an SDS-polyacrylamide gel electrophoresis using Novex™ 4-20% Tris-Glycine Mini Gel (Invitrogen, XP04200PK2) and transferred to PVDF membrane (Millipore, IPVH304F0). The membrane was blocked in blocking buffer with 10% horse serum to prevent non-specific binding, followed by incubation with different antibodies: SLC25A1 (Santa Cruz, sc-86392 or Proteintech, 15235-1-AP), ACC1 (Cell Signaling, #3676), FASN (Cell Signaling, #3180), IDH1 (Proteintech, 12332-1-AP), pAMPK-α (Cell Signaling, #2535), IDH1 (Proteintech, 12332-1-AP), p21 Waf1/Cip1 (Cell Signaling, #37543), mTOR (Cell Signaling, #2983), pH2A.X (Cell Signaling, #9718), GLS1 (Proteintech, 15235-1-AP), p53 (Santa Cruz, sc-126 and Sigma Aldrich, OP29-100UG). Appropriate horseradish peroxidase–conjugated secondary antibody (Invitrogen) was applied after incubation with primary antibody, SuperSignal™ West Pico PLUS Chemiluminescent Substrate (Thermo Scientific, 34577) or SuperSignal™ West Dura Extended Duration Substrate (Thermo Scientific, 34075) were used for protein detection. β-Actin (Santa Cruz, sc-47778) and HSP70 (Santa Cruz, sc-24) served as a loading control.

Quantitative real-time PCR. Total RNA was extracted from frozen tissue and cells pellet samples using TRIzol™ Reagent (Invitrogen, 15596026), followed by RNA quantification with NanoDrop (Implen, Munich, Germany). After genomic DNA treatment by DNase I (Invitrogen, AM2222), total RNA was used in cDNA synthesis with SuperScript™ IV Reverse Transcriptase (Invitrogen, 18090200) and random hexamers according to the manufacturer's instructions. The quantitative Reverse Transcriptase-PCR (qRT-PCR) was performed on the QuantStudio™ 12K Flex Real-Time PCR System (Applied Biosystems) with PowerUp™ SYBR Green Master Mix (Applied Biosystems). The obtained results were normalized to housekeeping genes, and their sequences are listed in Table S1.

RNA sequencing. Brains isolated from 18.5 dpf embryos were used for RNA sequencing. Briefly, total RNA was isolated using RNAeasy Mini kit (Qiagen, Hilden, Germany) according to the manufacturer's instructions. RNA sequencing (RNAseq) was performed by Novogene. Raw intensity data was background corrected and filtered of low expression genes across samples (low expression genes across samples (low expression genes

across samples (<100 read) prior to analysis. Normalization and differential expression were performed in R using the DESeq2 package. A cutoff of $p < 0.05$ and $|FC| > 2$ were used to determine differentially expressed genes. The GSEA Java-based software package from The Broad Institute was used to identify top enriched pathways in *Slc25a1*$^{+/+}$ and *Slc25a1*$^{-/-}$ brains. Reference genome and gene model annotation files were downloaded from genome website directly. Index of the reference genome was built using Hisat2 v2.0.5 and paired-end clean reads were aligned to the reference genome using Hisat2 v2.0.5. featureCounts v1.5.0-p3 was used to count the reads numbers mapped to each gene. FPKM of each gene was calculated based on the length of the gene and reads countmapped to this gene. FPKM, expected number of Fragments Per Kilobase of transcript sequence per Millions base pairs sequenced, considers the effect of sequencing depth and gene length for the reads count at the same time, and is currently the most commonly used method for estimating gene expression levels. Differential expression analysis was performed using the DESeq2 R package (1.20.0). The P values were adjusted using the Benjamini & Hochberg method. Corrected P-value of 0.05 and absolute fold change of 2 were set as the threshold for significantly differential expression. Enrichment analysis of differentially expressed genes.

Immunohistochemistry and immunofluorescence. Age-matched/embryos were removed from the uteri and fixed in 4% paraformaldehyde in phosphate-buffered saline and paraffin embedded, sectioned in the mid sagittal plane and stained with hematoxylin and eosin (H&E) and anti-Slc25a1 antibody (Proteintech, 15235-1-AP), used at 1/150 dilution. Consecutive sections with the primary antibody omitted were used as negative controls. Stained slides were scanned using the VS120 Virtual Slide Microscope (Olympus). For immunofluorescence (IF) staining, FFPE embryo sections were deparaffinized and sodium citrate was used for antigen retrieval. Slides were washed in PBS, blocked using TBST+20% Aquablock, and incubated with primary antibodies: anti-Slc25a1 (Proteintech, 15235-1-AP), mitofilin (Santa Cruz, sc-390707), p21 (Santa Cruz, sc-756). Finally, samples were washed in PBST and incubated with appropriate secondary antibody and DAPI or Hoechst (Sigma-Aldrich). IF samples were acquired using a Zeiss LSM800 laser scanning confocal microscope and analyzed using ImageJ/Fiji software.

Senescence-associated β-Gal staining. Cells grown on a 6-well plate were washed with PBS, fixed with fixative solution and stained with x-gal according to the manufacturer protocol (Cell Signaling, #9860). After

counterstaining with DAPI, cells were imaged using an Olympus IX-71 Inverted Epifluorescence Scope and multiple images of each well were taken for quantification.

Seahorse extracellular flux analyzer measurements. Cells were seeded at 10 000 cells/well density in high glucose DMEM with 10% FBS, 1 mM pyruvate and 1% antibiotic solution, and the following day treated with the indicated drug/vehicle for 24 h. Seahorse measurements were done according to the manufacturer's instructions, briefly: for the mitochondrial stress test, the medium was replaced with DMEM without FBS or bicarbonate, containing 5 mM glucose, 1 mM pyruvate, 2 mM glutamine and placed in a CO2 free incubator at 37 °C for 1 h, transferred to the Xf96 extracellular flux analyzer (Agilent). The program consisted of three measurements of OCR/ECAR before the injection of each drug: oligomycin (0.5 μM final concentration), FCCP (2 μM) and rotenone/antimycin (0.5 μM of each).

2HG analysis. The α-Hydroxyglutaric Acid was obtained from Cayman Chemicals. Diacetyl-L-tartaric anhydride (DATAN) was purchased from FisherScientific. All other reagents and solvents were of analytical and LCMS grade. Sample preparation: a volume of 50 μL from amniotic fluid was extracted with 250 μL of methanol containing 0.004 mmol/L of the internal standard (IS). Cell pellets were extracted with a volume of 1 mL of methanol containing 0.004 mmol/L of the internal standard. Samples were centrifuged for 20 minutes at 14, 000 X g and 4 °C. The supernatant was separated in a clean set of vials. The vial contents were evaporated to dryness at 22 °C by a gentle flow of nitrogen. The di-acetyltartaryl derivative was prepared by treating the dry residue with 50 μL of freshly made 50 mg/mL DATAN in Acetonitrile–acetic acid (4:1 by volume). The vials were capped and heated at 75 °C for 60 minutes. After the vial were cooled to room temperature, the mixture was evaporated to dryness by a nitrogen stream at room temperature, the residue was redissolved in 100 μL of distilled water, and 10 μL of the aqueous solution was injected on the LC column and analyzed by LCMS. The sample, prepared in the first step, were analyzed on a Sciex QTRAP 4500 mass spectrometer equipped with a Shimadzu Prominence UFLC XR System whereas, it was separated Phenomenex Lux 3 μm AMP, LC Column 150 x 3.0 mm, PN: 00F-4751-Y0. The column temperature was kept at 22 0C. Solvent A was 100% LCMS grade water with 0.1% formic acid and solvent B was 100% LCMS grade acetonitrile with 0.1% formic acid. The source temperature was kept at kept at 220 0C. The ion spray voltage was -4500 volts. The flow rate was consent throughout the method and was set to 0.3 mL/min. The mass spectrometry method was

set to a Negative MRM mode with a cycle time of 0.99 second. The targeted masses of the derivatized 2-HG were m/z 363, 147, and 129 Da. The Entrance Potential (EP) was set to -10 volts and the Declustering Potential (DP), the Collision Cell Exit Potential (CXP) were set to values optimized previously for each and every assigned transition. The concentration of the analyte in urine was calculated by interpolation of the observed analyte/IS peak-area ratio based on the linear regression line for the calibration curve, which was obtained by plotting peak-area ratios vs analyte concentration. Data was analyzed using Analyst 1.7 and Sciex OS software for quantification.

D/L-2HG Derivatization method. The α-Hydroxyglutaric Acid was obtained from Cayman Chemicals. Diacetyl-L-tartaric anhydride (DATAN) was purchased from FisherScientific. All other reagents and solvents were of analytical and LCMS grade. A volume of 50 µL from amniotic fluid was extracted with 250 µL of methanol containing 0.004 mmol/L of the internal standard (IS). Cell pellets were extracted with a volume of 1 mL of methanol containing 0.004 mmol/L of the internal standard. Samples were centrifuged for 20 minutes at 14, 000 X g and 4 °C. The supernatant was separated in a clean set of vials. The vial contents were evaporated to dryness at 22 °C by a gentle flow of nitrogen. The di-acetyltartaryl derivative was prepared by treating the dry residue with 50 µL of freshly made 50 mg/mL DATAN in Acetonitrile–acetic acid (4:1 by volume). The vials were capped and heated at 75 °C for 60 minutes. After the vial were cooled to room temperature, the mixture was evaporated to dryness by a nitrogen stream at room temperature, the residue was redissolved in 100 µL of distilled water, and 10 µL of the aqueous solution was injected on the LC column and analyzed by LCMS. The sample, prepared in the first step, were analyzed on a Sciex QTRAP 4500 mass spectrometer equipped with a Shimadzu Prominence UFLC XR System whereas, it was separated Phenomenex Lux 3 µm AMP, LC Column 150 x 3.0 mm, PN: 00F-4751-Y0. The column temperature was kept at 22 0C. Solvent A was 100% LCMS grade water with 0.1% formic acid and solvent B was 100% LCMS grade acetonitrile with 0.1% formic acid. The source temperature was kept at kept at 220 0C. The ion spray voltage was -4500 volts. The flow rate was consent throughout the method and was set to 0.3 mL/min. The mass spectrometry method was set to a Negative MRM mode with a cycle time of 0.99 second. The targeted masses of the derivatized 2-HG were m/z 363, 147, and 129 Da. The Entrance Potential (EP) was set to -10 volts and the Declustering Potential (DP), the Collision Cell Exit Potential (CXP) were set to values optimized previously for each and

every assigned transition. The concentration of the analyte in urine was calculated by interpolation of the observed analyte/IS peak-area ratio based on the linear regression line for the calibration curve, which was obtained by plotting peak-area ratios vs analyte concentration. Data was analyzed using Analyst 1.7 and Sciex OS software for quantification.

Zebrafish. All zebrafish procedures were performed in accordance with NIH guidelines for the maintenance and use of laboratory animals and approved by the Georgetown University Institutional Animal Care and Use Committee Protocol #2017-0078. Mixed wild-type, or *mitfa*$^{w2/w2}$*; mpv17* $^{a9/a9}$ (casper), embryos were obtained by pair-wise and group breeding, and raised in fish water (0.3 g/L sea salts) at 28°C. For drug treatments, (2R)-Octyl-α-hydroxyglutarate (Cayman Chemicals) and (2S)-Octyl-α-hydroxyglutarate (Cayman Chemicals), solutions were prepared in fish water. Embryos were treated at blastula, 1 dpf, or 2 dpf stages at a density of 100ul drug solution per embryo. Chorions were removed at 1 dpf by 10 min incubation in 200ug/ml pronase. Drug solutions were replaced daily. SA–β–GAL staining was performed as described (Da Silva-Álvarez et al., 2020) modified with the replacement of X-gal with Bluo-Gal, 5-Bromo-3-indolyl β-D-galactopyranoside.

Statistical analyses. For the analysis of the RNAseq experiments in the brain, differentially Expressed Genes were obtained using DESeq2 (2). Significantly upregulated Genes (FDR < 0.05) were assessed for pathway enrichment using the Reactome 2022 database (5) via EnrichR (4). Significantly enriched Pathways were clustered via GeneSetCluster(3) using a distance score that reflects similarities in genes mapping to multiple significantly enriched pathways. Similar processes were summarized by secondary annotation. To identify similarities between pathways unregulated in our data set, and the data available from other studies with IDH1/IDH2 mutants, GeoExplorer[1] was used to perform differential expression analysis of microarray data from GSE54838 and GSE85080 datasets. Significantly upregulated genes with the *IDH1/2* KI were assessed for pathway enrichment using the same method as previously described. Overlap of enriched pathways between *Slc25a1*$^{-/-}$ brains (this study) and that of the IDH1/2 KI data were assessed via a two-tailed fisher's exact test. The p-values of Reactome pathway enrichment were displayed as a Heatmap via GraphPad Prism. For all experiments, results are presented as mean value ±SD or SEM, unless specified otherwise. Statistical significance was assessed using unpaired non parametric t-test, unless indicated otherwise. Significant

differences were graphed using GraphPad Prism software and $p < 0.05$ was considered as statistically significant.

Study approval. All animal studies were conducted in compliance with ethical regulations according to protocol #2017-1192 approved by the Institutional Animal Care and Use Committee (IACUC) at Georgetown University. All the mice were housed at Georgetown University Division of Comparative Medicine, in a SPF vivarium which is maintained at a 12:12 h light:dark cycle, at 68–74°F and 30–70% humidity range. Mice were euthanized according to the IACUC guidelines. Patients 897 and 893 were treated under compassionate drug use protocols approved by the University of Pittsburgh and University of Mississippi IRBs. The collection of fibroblasts was approved by the Institutional Review Board at the University of Pittsburgh, protocol #19090211.

Data availability. All data will be made available on public databases and upon request.

Authors contribution. MLA designed the non-patient studies and wrote the paper. JV accrued the patients, designed all the patient studies, accrued patient-derived cells and wrote all the clinical data. AKP performed the majority of the non-patient experiments, organized the data for the Figures and proof-edited the manuscript for accuracy in the description of the experiments. MT generated the mouse colonies and worked with AKP for three years on this project. YLP performed the patient oriented studies, the metabolomic studies, and the seahorse experiments on the patient cells. RR performed the IHC and the IF experiments. AMI designed and performed the statistical analyses. HF performed the Seahorse experiments in the *Slc25a1*$^{-/-}$ MEFs and contributed to the initial functional characterization of the mice-derived cells. RM has maintained all the mouse strains during Covid 19, and performed several experiments. MG developed the method for the chiral derivatization of D/L-2HG and performed the experiments for enantiomer identification in murine and patient cells. AC helped with the interpretation of the metabolomic and lipidomic data. LJ performed isotope tracing experiment to identify 2HG enrichment from glutamine. LFK provided interpretation for the H&E on the murine brain samples. AP and CC performed the SEM experiments and provided interpretation. BK provided access to JV from his patients. GP provided expertise and supervision to RR with the IF experiments. EG and MLA designed the experiments in zebrafish, EG performed the experiments, assembled the Figures and provided interpretation of the results. CA provided expertise in the interpretation of the phenotype and of the CT scans of the mice, proof-edited the manuscript and offered inputs on this project throughout the years.

Acknowledgements. Studies on SLC25A1 in the MLA lab have been supported by R01CA193698, R21DE028670 and R21CA256546. JV is the Cleveland Family Endowed Chair in Pediatric Research with support in part from NIH grant R01DK109907. YLP was an ABMGG Clinical Biochemical Genetics fellow supported by a pilot project grant 20(GG014929-16) from North American Mitochondrial Disease Consortium under the Rare Diseases Clinical Research Network and a Rangos Advisory Committee fellowship grant from UPMC Children's Hospital of Pittsburgh. We acknowledge our patients and families for their participation in this study; Dr. Johan Van Hove for advice on the NAMDC IRB application, the University of Pittsburgh Rangos Metabolic Core services, Center for Research Computing and the clinical diagnostic services provided by the General Genetics Clinic and Clinical Biochemical Genetics Laboratory. We are grateful to Dr. Anton Wellstein for inputs on this project, to the Riegel/Wellstein and to Dr. Chunling Yi laboratories for sharing reagents and instrumentation. We thank Sarah Flowers for her inputs on all of the projects related to SCL25A1. Shreyas Gadre performed some of the experiments in the MLA's laboratory.

References.

1. Mosaoa R, et al. The Mitochondrial Citrate Carrier SLC25A1/CIC and the Fundamental Role of Citrate in Cancer, Inflammation and Beyond. *Biomolecules*. 2021;11(2):141. doi:10.3390/biom11020141

2. Palmieri F, Scarcia P, Monné M. Diseases Caused by Mutations in Mitochondrial Carrier Genes *SLC25*: A Review. *Biomolecules*. 2020;10(4):655. doi:10.3390/biom10040655

3. Ruprecht JJ, Kunji ERS. The SLC25 Mitochondrial Carrier Family: Structure and Mechanism. *Trends Biochem Sci*. 2020;45(3):244-258. doi:10.1016/j.tibs.2019.11.001

4. Maynard TM, et al. Mitochondrial localization and function of a subset of 22q11 deletion syndrome candidate genes. *Mol Cell Neurosci*. 2008;39(3):439-451. doi:10.1016/j.mcn.2008.07.027

5. Funato N. Craniofacial Phenotypes and Genetics of DiGeorge Syndrome. *J Dev Biol*. 2022;10(2):18. doi:10.3390/jdb10020018

6. Catalina-Rodriguez O, et al. The mitochondrial citrate transporter, CIC, is essential for mitochondrial homeostasis. *Oncotarget*. 2012;3(10):1220-1235. doi:10.18632/oncotarget.714

7. Chaouch A, et al. Mutations in the Mitochondrial Citrate Carrier SLC25A1 are Associated with Impaired Neuromuscular Transmission. *J Neuromuscul Dis*. 2014;1(1):75-90. doi:10.3233/JND-140021

8. Prasun P, et al. Expanding the Clinical Spectrum of Mitochondrial Citrate Carrier (SLC25A1) Deficiency: Facial Dysmorphism in Siblings with Epileptic Encephalopathy and Combined D,L-2-Hydroxyglutaric Aciduria. *JIMD Rep*. 2015;19:111-115. doi:10.1007/8904_2014_378

9. Nota B, et al. Deficiency in SLC25A1, encoding the mitochondrial citrate carrier, causes combined D-2- and L-2-hydroxyglutaric aciduria. *Am J Hum Genet*. 2013;92(4):627-631. doi:10.1016/j.ajhg.2013.03.009

10. Smith A, et al. Severe Neonatal Presentation of Mitochondrial Citrate Carrier (SLC25A1) Deficiency. *JIMD Rep*. 2016;30:73-79. doi:10.1007/8904_2016_536

11. Pop A, et al. An overview of combined D-2- and L-2-hydroxyglutaric aciduria: functional analysis of CIC variants. *J Inherit Metab Dis*. 2018;41(2):169-180. doi:10.1007/s10545-017-0106-7

12. Edvardson S, et al. Agenesis of corpus callosum and optic nerve hypoplasia due to mutations in SLC25A1 encoding the mitochondrial citrate transporter. *J Med Genet*. 2013;50(4):240-245. doi:10.1136/jmedgenet-2012-101485

13. Kranendijk M, et al. Progress in understanding 2-hydroxyglutaric acidurias. *J Inherit Metab Dis*. 2012;35(4):571-587. doi:10.1007/s10545-012-9462-5

14. Du X, Hu H. The Roles of 2-Hydroxyglutarate. *Front Cell Dev Biol*. 2021;9:651317. doi:10.3389/fcell.2021.651317

15. Ježek P. 2-Hydroxyglutarate in Cancer Cells. *Antioxid Redox Signal*. 2020;33(13):903-926. doi:10.1089/ars.2019.7902

16. Losman JA, Kaelin WG Jr. What a difference a hydroxyl makes: mutant IDH, (R)-2-hydroxyglutarate, and cancer. *Genes Dev*. 2013;27(8):836-852. doi:10.1101/gad.217406.113

17. Cohen I, et al. A novel homozygous SLC25A1 mutation with impaired mitochondrial complex V: Possible phenotypic expansion. *Am J Med Genet A*. 2018;176(2):330-336. doi:10.1002/ajmg.a.38574

18. Fernandez HR, et al. The mitochondrial citrate carrier, SLC25A1, drives stemness and therapy resistance in non-small cell lung cancer. *Cell Death Differ*. 2018;25(7):1239-1258. doi:10.1038/s41418-018-0101-z

19. Ansó E, Weinberg SE, Diebold LP, et al. The mitochondrial respiratory chain is essential for haematopoietic stem cell function. *Nat Cell Biol*. 2017;19(6):614-625. doi:10.1038/ncb3529

20. Hunt RJ, et al. Mitochondrial stress causes neuronal dysfunction via an ATF4-dependent increase in L-2-hydroxyglutarate. *J Cell Biol*. 2019;218(12):4007-4016. doi:10.1083/jcb.201904148

21. Miller JJ. Targeting IDH-Mutant Glioma. *Neurotherapeutics*. 2022;19(6):1724-1732. doi:10.1007/s13311-022-01238-3

22. Dang L, Yen K, Attar EC. IDH mutations in cancer and progress toward development of targeted therapeutics. *Ann Oncol*. 2016;27(4):599-608. doi:10.1093/annonc/mdw013

23. Tommasini-Ghelfi S, et al. Cancer-associated mutation and beyond: The emerging biology of isocitrate dehydrogenases in human disease. *Sci Adv*. 2019;5(5):eaaw4543. doi:10.1126/sciadv.aaw4543

24. Tan M, et al. Inhibition of the mitochondrial citrate carrier, Slc25a1, reverts steatosis, glucose intolerance, and inflammation in preclinical models of NAFLD/NASH. *Cell Death Differ*. 2020;27(7):2143-2157. doi:10.1038/s41418-020-0491-6

25. Beigneux AP, et al. ATP-citrate lyase deficiency in the mouse. *J Biol Chem*. 2004;279(10):9557-9564. doi:10.1074/jbc.M310512200

26. Chirala SS, et al. Fatty acid synthesis is essential in embryonic development: fatty acid synthase null mutants and most of the heterozygotes die in utero. *Proc Natl Acad Sci U S A*. 2003;100(11):6358-6363. doi:10.1073/pnas.0931394100

27. Dickinson ME, et al. High-throughput discovery of novel developmental phenotypes [published correction appears in Nature. 2017 Nov 16;551(7680):398]. *Nature*. 2016;537(7621):508-514. doi:10.1038/nature19356

28. Groza T, et al. The International Mouse Phenotyping Consortium: comprehensive knockout phenotyping underpinning the study of human disease. *Nucleic Acids Res*. 2023;51(D1):D1038-D1045. doi:10.1093/nar/gkac972

29. Hirata M, et al. Mutant IDH is sufficient to initiate enchondromatosis in mice. *Proc Natl Acad Sci U S A*. 2015;112(9):2829-2834. doi:10.1073/pnas.1424400112

30. Sasaki M, et al. D-2-hydroxyglutarate produced by mutant IDH1 perturbs collagen maturation and basement membrane function. *Genes Dev*. 2012;26(18):2038-2049. doi:10.1101/gad.198200.112

31. Pirozzi CJ, et al. Mutant IDH1 Disrupts the Mouse Subventricular Zone and Alters Brain Tumor Progression. *Mol Cancer Res*. 2017;15(5):507-520. doi:10.1158/1541-7786.MCR-16-0485

32. Akbay EA, et al. D-2-hydroxyglutarate produced by mutant IDH2 causes cardiomyopathy and neurodegeneration in mice. *Genes Dev*. 2014;28(5):479-490. doi:10.1101/gad.231233.113

33. Jiang L, et al. Reductive carboxylation supports redox homeostasis during anchorage-independent growth. *Nature*. 2016;532(7598):255-258. doi:10.1038/nature17393

34. Jiang L, et al. Quantitative metabolic flux analysis reveals an unconventional pathway of fatty acid synthesis in cancer cells deficient for the mitochondrial citrate transport protein. *Metab Eng*. 2017;43(Pt B):198-207. doi:10.1016/j.ymben.2016.11.004

35. Cheng QY, et al. Sensitive Determination of Onco-metabolites of D- and L-2-hydroxyglutarate Enantiomers by Chiral Derivatization Combined with Liquid Chromatography/Mass Spectrometry Analysis. *Sci Rep*. 2015;5:15217. doi:10.1038/srep15217

36. Rhinn M, et al. Aberrant induction of p19Arf-mediated cellular senescence contributes to neurodevelopmental defects. *PLoS Biol*. 2022;20(6):e3001664. doi:10.1371/journal.pbio.3001664

37. Storer M, et al. Senescence is a developmental mechanism that contributes to embryonic growth and patterning. *Cell*. 2013;155(5):1119-1130. doi:10.1016/j.cell.2013.10.041

38. Klein A, Rhinn M, Keyes WM. Cellular senescence and developmental defects. *FEBS J*. 2023;290(5):1303-1313. doi:10.1111/febs.16731

39. Papadopoli D, et al. mTOR as a central regulator of lifespan and aging. *F1000Res*. 2019;8:F1000 Faculty Rev-998. doi:10.12688/f1000research.17196.1

40. Kumari R, Jat P. Mechanisms of Cellular Senescence: Cell Cycle Arrest and Senescence Associated Secretory Phenotype. *Front Cell Dev Biol*. 2021;9:645593. doi:10.3389/fcell.2021.645593

41. Bernadotte A, Mikhelson VM, Spivak IM. Markers of cellular senescence. Telomere shortening as a marker of cellular senescence. *Aging (Albany NY)*. 2016;8(1):3-11. doi:10.18632/aging.100871

42. Weichhart T. mTOR as Regulator of Lifespan, Aging, and Cellular Senescence: A Mini-Review. *Gerontology*. 2018;64(2):127-134. doi:10.1159/000484629

43. Wiley CD, et al. Mitochondrial Dysfunction Induces Senescence with a Distinct Secretory Phenotype. *Cell Metab*. 2016;23(2):303-314. doi:10.1016/j.cmet.2015.11.011

44. Böttcher M, et al. D-2-hydroxyglutarate interferes with HIF-1α stability skewing T-cell metabolism towards oxidative phosphorylation and impairing Th17 polarization. *Oncoimmunology*. 2018;7(7):e1445454. doi:10.1080/2162402X.2018.1445454

45. Fu X, et al. 2-Hydroxyglutarate Inhibits ATP Synthase and mTOR Signaling. *Cell Metab*. 2015;22(3):508-515. doi:10.1016/j.cmet.2015.06.009

46. Lutze G, et al. Non-canonical WNT-signaling controls differentiation of lymphatics and extension lymphangiogenesis via RAC and JNK signaling. *Sci Rep*. 2019;9(1):4739. doi:10.1038/s41598-019-41299-7

47. Mühlhausen C, et al. Combined D2-/L2-hydroxyglutaric aciduria (SLC25A1 deficiency): clinical course and effects of citrate treatment. *J Inherit Metab Dis*. 2014;37(5):775-781. doi:10.1007/s10545-014-9702-y

48. Salamanca-Cardona L, et al. In Vivo Imaging of Glutamine Metabolism to the Oncometabolite 2-Hydroxyglutarate in IDH1/2 Mutant Tumors. *Cell Metab*. 2017;26(6):830-841.e3. doi:10.1016/j.cmet.2017.10.001

49. Wise DR, et al. Hypoxia promotes isocitrate dehydrogenase-dependent carboxylation of α-ketoglutarate to citrate to support cell growth and viability. *Proc Natl Acad Sci U S A*. 2011;108(49):19611-19616. doi:10.1073/pnas.1117773108

50. Kormanik K, et al. Evidence for involvement of medium chain acyl-CoA dehydrogenase in the metabolism of phenylbutyrate. *Mol Genet Metab*. 2012;107(4):684-689. doi:10.1016/j.ymgme.2012.10.009

51. Berry SA, et al. Safety and efficacy of glycerol phenylbutyrate for management of urea cycle disorders in patients aged 2months to 2years. *Mol Genet Metab*. 2017;122(3):46-53. doi:10.1016/j.ymgme.2017.09.002

52. Zhao J, et al. Metabolic remodelling during early mouse embryo development. *Nat Metab*. 2021;3(10):1372-1384. doi:10.1038/s42255-021-00464-x

53. Smolková K, et al. Reductive carboxylation and 2-hydroxyglutarate formation by wild-type IDH2 in breast carcinoma cells. *Int J Biochem Cell Biol*. 2015;65:125-133. doi:10.1016/j.biocel.2015.05.012

54. Tommasini-Ghelfi S, et al. Cancer-associated mutation and beyond: The emerging biology of isocitrate dehydrogenases in human disease. *Sci Adv*. 2019;5(5):eaaw4543. doi:10.1126/sciadv.aaw4543

55. Karlstaedt A, et al. Oncometabolite d-2-hydroxyglutarate impairs α-ketoglutarate dehydrogenase and contractile function in rodent heart. *Proc Natl Acad Sci U S A*. 2016;113(37):10436-10441. doi:10.1073/pnas.1601650113

56. Ma S, et al. *L2hgdh* Deficiency Accumulates l-2-Hydroxyglutarate with Progressive Leukoencephalopathy and Neurodegeneration. *Mol Cell Biol*. 2017;37(8): e00492-16.

57. Sears TK, Horbinski CM, Woolard KD. IDH1 mutant glioma is preferentially sensitive to the HDAC inhibitor panobinostat. *J Neurooncol*. 2021;154(2):159-170. doi:10.1007/s11060-021-03829-0

58. Chang CM, et al. Mutant Isocitrate Dehydrogenase 1 Expression Enhances Response of Gliomas to the Histone Deacetylase Inhibitor Belinostat. *Tomography*. 2023;9(3):942-954. doi:10.3390/tomography9030077

Figure Legends

Figure 1. Characteristics of patients identified in this study and analysis of SLC25A1 protein expression.

(**A**) General scheme of the TCA cycle and mode of action of SLC25A1. The structure of αKG and D/L-2HG is shown in boxes.

(**B**) Magnetic Resonance Imaging of the brain of Patient 897. There is a large defect in the septum pellucidum and optic nerves were not well seen (upper panels and lower left panel, indicated by arrow). White matter loss, with moderate to severe supratentorial ventriculomegaly and irregular margins of the lateral ventricles are indicated by arrows (right lower panel). The corpus callosum is markedly thinned but does appear to be present.

(**C**) SLC25A1 protein expression in control and patient derived fibroblasts.

(**D**) Expression levels of SLC25A1 protein in the indicated organs derived from two *Slc25a1* wild-type embryos at E19.5 dpf.

(**E and F**) Representative IHC images with the anti-SLC25A1 antibody staining in embryos at E19 dpf. Cb= Cerebellum, Cx= Cerebral cortex, F=follicle, P=palate, T=tongue, M=mandible, NB= nasal bone, NC= nasal cavity, OL=olfactory lobe, ON=olfactory nerve.

(**G**) Slc25a1, DAPI and mitofilin protein expression in embryos at E19 dpf. Bar=1000 μm.

Figure 2. The knock-out of the *Slc25a1* gene leads to lethality to a heterogenous pattern of abnormalities.

(**A**) Representative immunoblot showing the SLC25A1 protein expression in MEFs cells isolated from *Slc25a1*$^{+/+}$, *Slc25a1*$^{+/-}$ and *Slc25a1*$^{-/-}$ embryos (n=3 per genotype).

(**B**) Representation of the genotypes observed across 85 litters (495 mice) obtained by breeding *Slc25a1* heterozygous mice.

(**C**) Number and percentage of births observed across a population of newborn *Slc25a1*$^{-/-}$ mice.

(**D**) Prevalence of the phenotypic alterations observed in *Slc25a1*$^{-/-}$ embryos.

(**E**) Representative images of *Slc25a1*$^{+/+}$, *Slc25a1*$^{+/-}$ and *slc25a1*$^{-/-}$ embryos under stereoscopic microscope at E18.5 dpf. Red arrows point to cleft palate, underdeveloped ears and brain abnormalities. Bar=5 mm.

(**F**) Measurements of crows to rump length showing smaller body size in *Slc25a1* homozygous mice compared with wild-type and heterozygous littermates (n= 16 mice per genotype, respectively). p-values were calculated with two tailed non parametric t-test.

(**G**) Heterogeneity of the phenotypes of *Slc25a1*$^{-/-}$ embryos, showing variations in body size, lack of skull and eyes in the last two embryos on left. Embryos 1-3 and 4-5 are from the same litters.

(**H**) Computed Tomography (CT) scan of wild-type or *Slc25a1*$^{-/-}$ embryos at E18.5 dpf. Yellow numbers indicate: 1: Excencephaly; 2: Protruding tongue; 3: Gastroschisis; 4: Pectus excavatum; 5: Abnormal heart. 6: Abnormal eye; 7: Abnormal facial area morphology. Bar=1mm.

(**I**) Representative images of H&E staining in the embryos of the indicated genotype. Top panels show the anatomy of the whole head; lower panels show magnification of the cortical region and nuclear abnormalities in *Slc25a1*$^{-/-}$ mice. Bar= 20 µm.

(**J**) Scanning electron microscopy (SEM) overviews of the indicated tissues (see also text for explanation) of wild-type and *Slc25a1*$^{-/-}$ embryos at E18.5 dpf.

Figure 3. Loss of SLC25A1 leads to metabolic remodeling.

(**A-B**) Expression of indicated proteins in brain (A) and MEFs (B) isolated from *Slc25a1*$^{+/+}$, *Slc25a1*$^{+/-}$ and *Slc25a1*$^{-/-}$ embryos (n=3 per genotype).

(**C**) mRNA levels detected with q-RT-PCR of the indicated genes in MEFs *Slc25a1*$^{+/+}$ (gray) and *Slc25a1*$^{-/-}$ (red). Each dot is a different mouse in 3 replicates.

(**D**) Heatmap of top 25 enriched lipids in brain samples obtained from *Slc25a1*$^{+/+}$ (green) and *Slc25a1*$^{-/-}$ (red) (n=5, from different litters, each in triplicate). Normalization was performed by dividing area under the curve for each metabolite by internal standard area. Clustering was performed by using the Metaboanalyst software.

(**E-F**) Pathway enrichment analysis in amniotic fluid obtained from *Slc25a1*$^{-/-}$ embryos (E) (n=3 per genotype, each in 3 technical replicates) and patient fibroblasts relative to control (F).

(**G)** Enrichment analysis in the patient fibroblast using the Metaboanalyst software obtained by inputting the lipid species identified with untargeted metabolomic analysis.

(**H**) Volcano plot of metabolites detected with untargeted metabolomic analysis and altered in a mix of extracts derived from both patient's fibroblasts versus control fibroblasts. The position of citrate, αKG and 2-HG is shown.

(**I**) TCA intermediates in the amniotic fluid obtained from *Slc25a1*$^{+/+}$ (blue) and *Slc25a1*$^{-/-}$ (red) embryos (n=3-5, each in technical replicates).

(**J**) Pathway enrichment analysis in brain samples obtained from *Slc25a1*$^{+/+}$ and *Slc25a1*$^{-/-}$ embryos (n=5, per genotype).

Unpaired non parametric t-test was used throughout.

Figure 4. *Slc25a1*$^{-/-}$ brains mimic an IDH1/2 mutant transcriptome.

(**A-B**) 2HG enrichment in the amniotic fluid (A) and brain samples (B) obtained from *Slc25a1*$^{+/+}$ (blue) and *Slc25a1*$^{-/-}$ (red) embryos at E18.5 dpf (n=4).

(**C**) D- and L- 2HG enrichment in the amniotic fluid samples obtained from *Slc25a1*$^{+/+}$ (blue) and *Slc25a1*$^{-/-}$ (red) embryos (n=4-5).

(**D**) Relative increase in D- and L- 2HG concentration (%) in the amniotic fluid samples obtained from *Slc25a1*$^{-/-}$ (red, n=3) embryos compared to their wild-type littermates (n=2).

(**E**) D-2HG enrichment in A549 cells harboring the shRNA mediated *SLC25A1* knock-down relative to control.

(**F**) Urine D- and L- 2HG concentration in patient samples. Data were extrapolated based on enrichment detected in two different studies. Patients 13-20 were from Ref. 11; Patients 1 and 2 from Ref. 8. The second patient in 8 showed inconsistent elevations of D/L-2HG in repeated urinalyses and only one measurement was used to calculate the percentage of D/L-2HG. Top numbers represent % enrichment.

(**G**) Venn diagram representing genes differentially regulated in the brains isolated from *Slc25a1*$^{+/+}$ and *Slc25a1*$^{-/-}$ embryos at 18.5 dpc (n=3).

(**H**) Hierarchical clustering map of differentially expressed genes as in G.

(**I**) Pathway enrichment analysis of genes significantly elevated in *Slc25a1*$^{-/-}$ mice relative to wild-type. All significantly enriched pathways (FDR<0.05), assessed from the Reactome Database, were clustered *via* a

distance metric derived from shared significant genes common amongst enriched gene sets. Clustered gene sets were summarized by biological function.

(**J**) GeoExplorer was used to perform differential expression analysis of microarray data from GSE54838 (heart, Ref. 33) and GSE85080 (CNS, Ref.32). Significantly upregulated genes with IDH1/2 KI were assessed for pathway enrichment using the Reactome 2022 database via EnrichR. Overlap of enriched pathways between *Slc25a1*$^{-/-}$ in this study and that of the IDH1/2 data were assessed via a two-tailed fisher's exact test. Dark green indicates a p-value below 0.05, light green indicates genes significantly upregulated and mapped to the same pathway, but not enough for enrichment; white indicates no significantly upregulated genes.

Created with biorender.

Figure 5. Loss of SLC25A1 induces senescence.

(**A**) Growth curves of MEF cells isolated from *Slc25a1*$^{+/+}$ and *Slc25a1*$^{-/-}$ embryos.

(**B-C**) Quantification of the SA-β-GAL positive MEF cells (%) normalized to the total number of cells identified with DAPI counter-staining pooled from two independent experiments and representative images of (SA-β-GAL) activity.

(**D-E**) Representative images of SA-β-GAL staining in human fibroblasts (D) and quantification of the SA-β-GAL positive cells normalized to the total number of cells identified with DAPI counter-staining (E). Data are presented as a % positive cells ± SD pooled from two independent experiments. Bar=100 µm.

(**F-G**) Expression of the indicated proteins in MEFs obtained from *Slc25a1*$^{+/+}$, *Slc25a1*$^{+/-}$ and *Slc25a1*$^{-/-}$ embryos (F), patient's fibroblasts (G).

(**H**) mRNA levels of the indicated genes in MEFs *Slc25a1*$^{+/+}$ (grey) and *Slc25a1*$^{-/-}$ (red) respectively (n=3-4).

(**I-J**) Protein (I) and mRNA levels (J) of the indicated senescence markers.

(**K**) p21 immunofluorescence staining of the head of *Slc25a1*$^{+/+}$ and *Slc25a1*$^{-/-}$ embryos (E19 dpf). Hoechst was used to counterstain nuclei. Secondary antibody alone was used as a control. Bar= 1000 µM.

SA-β-GAL staining was assessed by light microscopy. All results in this figure represent at least two independent experiments. Data are presented as mean value ± SD and p-values were calculated using unpaired non parametric t-test throughout.

Figure 6. 2HG induces mitochondrial respiratory deficit and senescence.

(**A-B**) Oxygen consumption rate (OCR) in MEFs isolated from *Slc25a1*$^{+/+}$ (black) and *Slc25a1*$^{-/-}$ (pink) (A) or in human fibroblasts (B). Data are presented as mean value ± SD by unpaired t-test. Injection of Oligomycin, FCCP and Rotenone/Antimycin (Rot/AA) allowed calculation of the BR= Basal respiration; ATP= ATP Production, MR= Maximal Respiration, SRC= Spare Respiratory Capacity.

(**C-D**) Oxygen consumption rate (OCR) was assessed using Seahorse Extracellular Flux Analyzer in human control fibroblasts treated with the indicated concentration of octyl-2HG for 24 hours. Bars represent the standard deviation and p-values were calculated using two tailed non parametric t-test.

(**E**)**.** Representative images of SA-β-GAL staining of control human fibroblast cells treated with indicated L-or D- 2HG for 72 hours (Bar= 100 μM).

(**F-H**) Quantification of SA-β-GAL staining of MEFs cells (F and H) or control human fibroblasts (G) treated with indicated concentrations of L-or D-2HG for 3 to 5 days (Bar= 100 μM).

(**I-J**) Expression levels of p53 and p21 in human fibroblast (G) or A549 cells (H) treated with L- and D-2HG alone or in combination.

Figure 7. 2HG perturbs embryonic development in zebrafish embryos.

(**A**) Phenotypes of 25 μM or 50 μM Octyl-R-2HG treated embryos at 2 dpf. Embryos were injected at blastula-stage. Prominent alterations are small eyes, bulging brains, enlarged yolk sack, pericardial edema, altered body curvature, reduced body length, lymphatic cysts, and disorganized cellular structure of tissues, most prominently seen in the brain.

(**B**) Phenotypes of 25 μM or 80 μM Octyl-R-2HG treated embryos at 36 hpf. Top embryo is control. Higher magnification images of the head show the dose-dependent tissue disorganization of the brain.

(**C**) Five days dpf Casper larvae. The top fish was treated with 30 μM Octyl-R-2HG plus 20 μM Octyl-S-2HG at 1 dpf. The lower fish is control. The treated larva has an enlarged heart (outlined with dashed line) and large diameter blood vessels (indicated with arrows). The treated larva additionally has a dysmorphic jaw and slightly bulging brain.

(**D**) SA-β-GAL, detected with Bluo-gal in the whole body (D) and brain (F) of embryos treated with 40 μM Octyl-S-2HG, showing enhanced activity in the brain, yolk, tail and around the eyes relative to control.

(**E**) Phenotype of 50 μM Octyl-S-2HG treated embryos at 3 dpf. Bottom embryo is control. Prominent arched phenotype along with bulging brain, small eye and large yolk.

(**F-G**) Phenotype of embryos treated with the indicated doses of Octyl-S-2HG at the indicated concentrations. Red arrows point to alterations in brain size, pericardial edema, enhanced body curvature and enlarged yolk (F). Treatment of embryos at 36 hpf, with the indicated mixtures using different ratios of Octyl-R-2HG and Octyl-S-2HG.

Figure 8. Positive effects of phenylbutyrate on Combined D/L-2HGA.

(**A**) Scheme representing the metabolic steps of conversion of phenylbutyrate into phenylacetyl-CoA and reaction with glutamine to form phenylacetylglutamine (PAG).

(**B**) Summary of the clinical improvements observed in patients treated with phenylbutyrate.

(**C**) Hierarchical distance clustering of the metabolomics data demonstrates that phenylbutyrate-treated FB893 and 897 fibroblasts have an improved metabolite profile that closely resembles the control fibroblasts.

(**D-E**) Volcano plot of metabolites altered in phenylbutyrate treated patients, demonstrating relevant reductions in the levels of αKG and 2HG and citrate accompanied by *de novo* formation of PAG. Individual changes are expressed in E.

(**F**) Enrichment analysis of top 50 down-regulated metabolites in patient samples treated with PB.

Figure 1

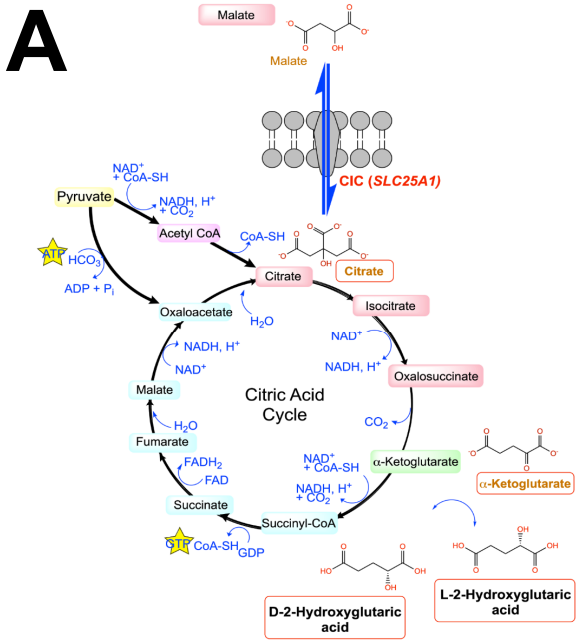
A
Malate
Malate
CIC (SLC25A1)
NAD+ + CoA-SH
Pyruvate
NADH, H+ + CO2
Acetyl CoA
CoA-SH
ATP
HCO3
ADP + Pi
Citrate
Citrate
Oxaloacetate
H2O
Isocitrate
NAD+
NADH, H+
NAD+
NADH, H+
Oxalosuccinate
Malate
Citric Acid Cycle
CO2
H2O
Fumarate
FADH2
FAD
NAD+ + CoA-SH
α-Ketoglutarate
α-Ketoglutarate
NADH, H+ + CO2
Succinate
Succinyl-CoA
GTP
CoA-SH
GDP
D-2-Hydroxyglutaric acid
L-2-Hydroxyglutaric acid

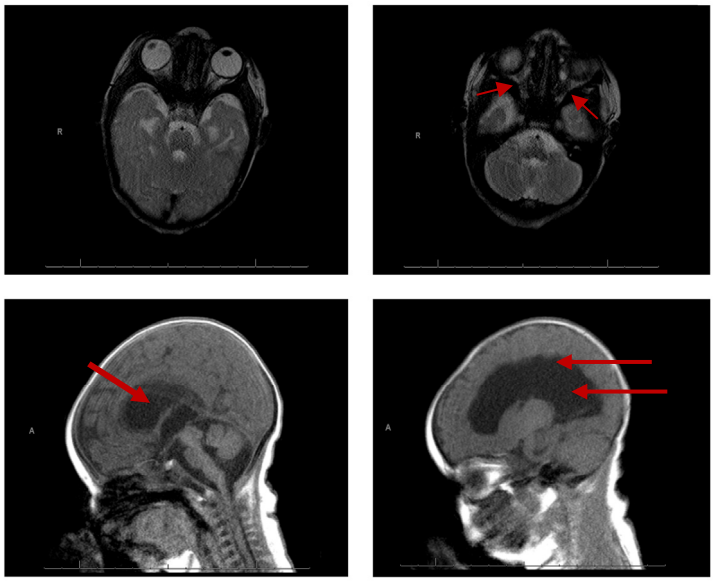
B

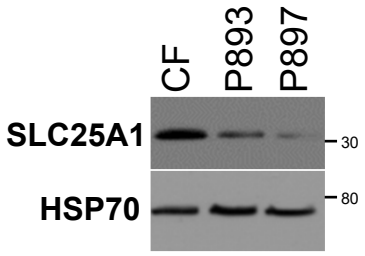
C
CF
P893
P897
SLC25A1
30
HSP70
80

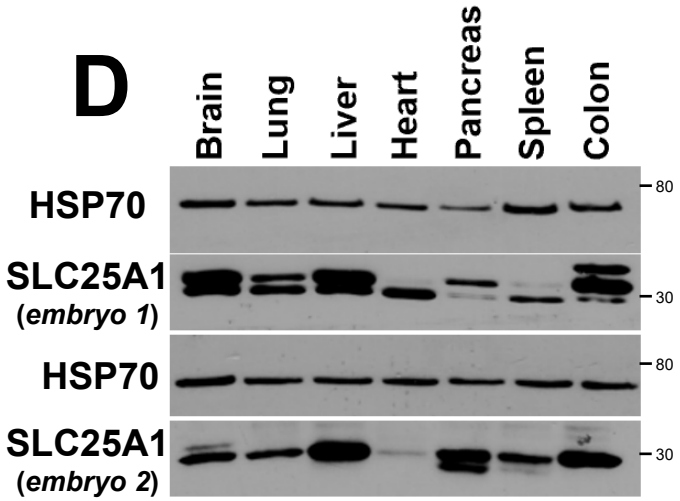
D
Brain
Lung
Liver
Heart
Pancreas
Spleen
Colon
HSP70
80
SLC25A1
(embryo 1)
30
HSP70
80
SLC25A1
(embryo 2)
30

E
5 mm

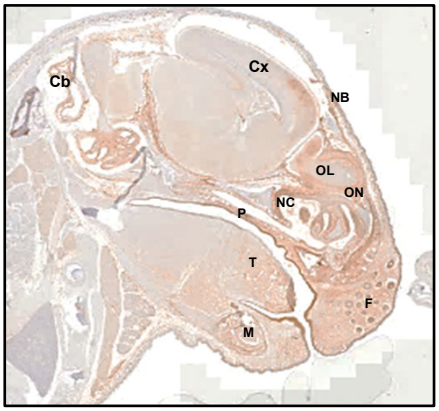
F
Cb
Cx
NB
OL
ON
NC
P
T
F
M

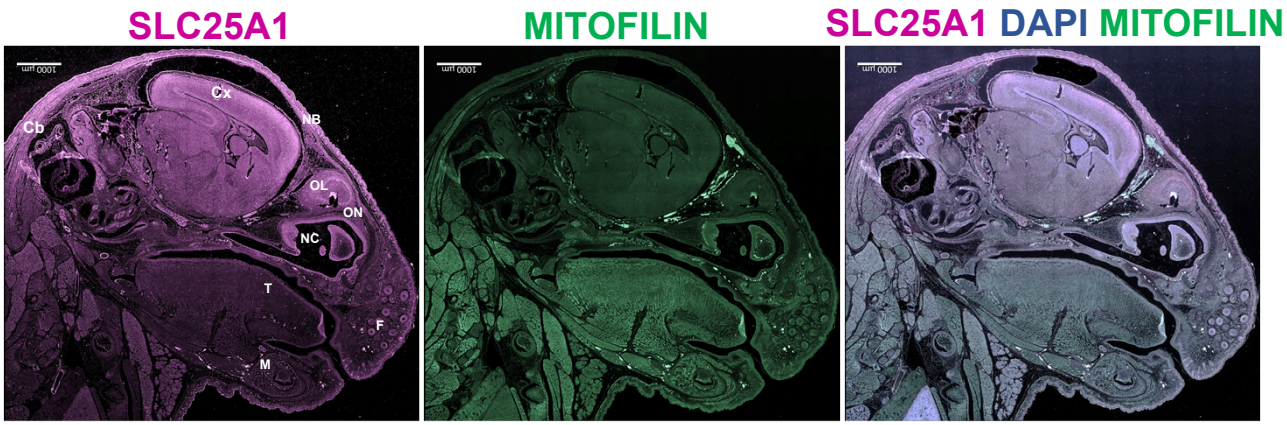
G
SLC25A1
MITOFILIN
SLC25A1 DAPI MITOFILIN
1000 µm
Cb
Cx
NB
OL
ON
NC
T
F
M

Figure 2

A

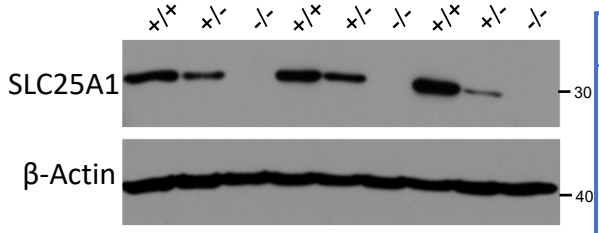

B

GT	Total	%
+/+	136	27
+/-	258	53
-/-	101	20
Tot.	495	

C

Births		
GT	Total #.	%
+/+	48	30.3
+/-	99	62.6
-/-	11	6.9
Total	158	

D

Phenotype	Total #	%
Exencephaly	36	43.90
Cleft palate/ flat face	40	48.78
Small size	62	75.61
Pale/anemic	23	28.05

E

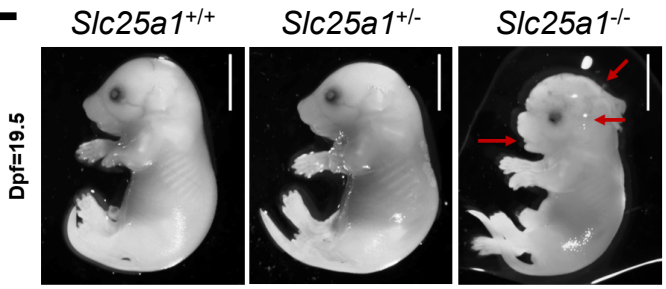

F

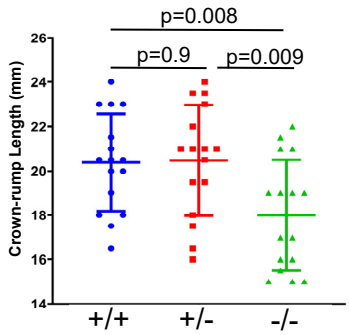

G

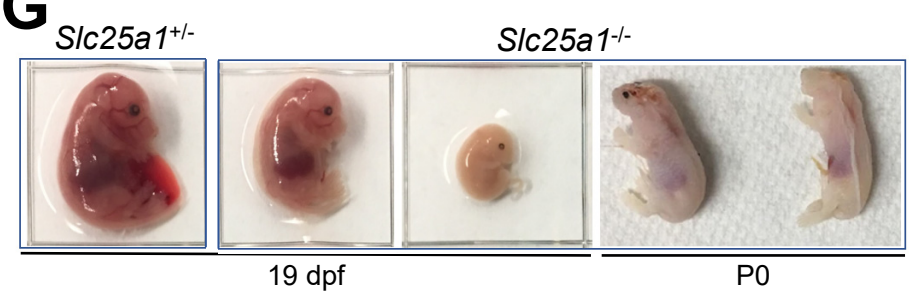

H

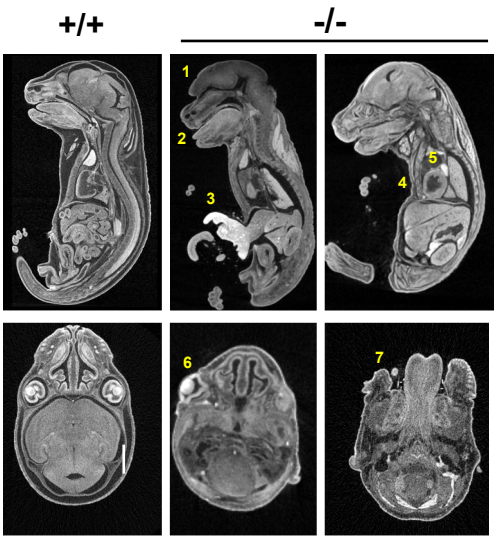

I

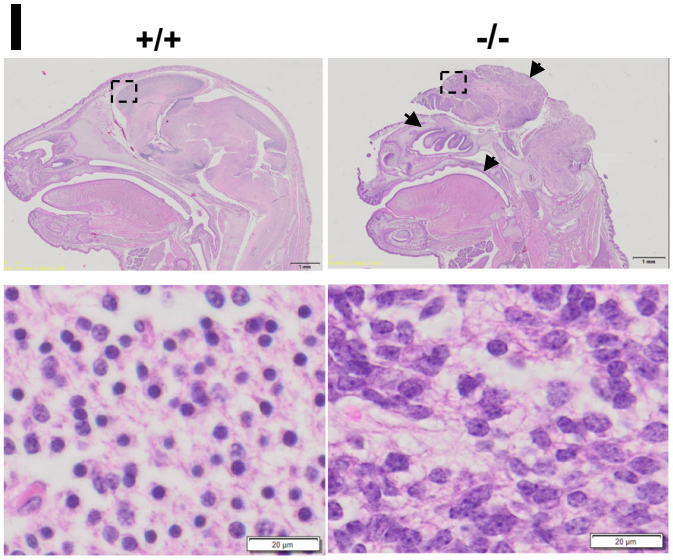

J

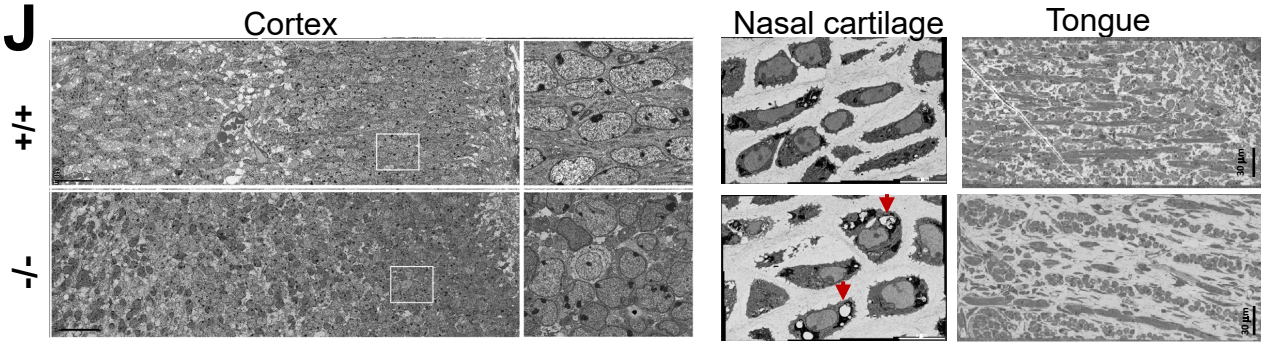

Figure 3

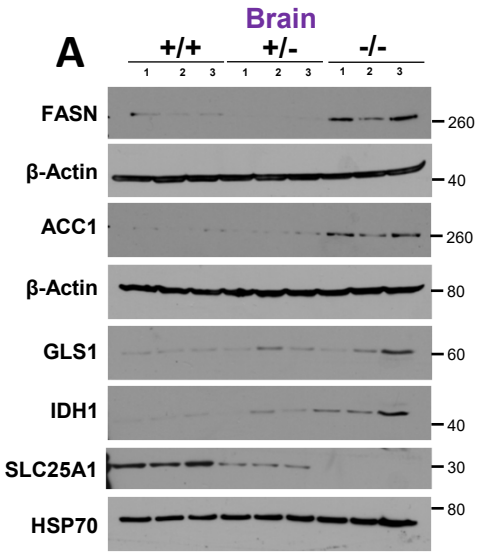
A
Brain
+/+
+/-
-/-
FASN
β-Actin
ACC1
β-Actin
GLS1
IDH1
SLC25A1
HSP70
260
40
260
80
60
40
30
80

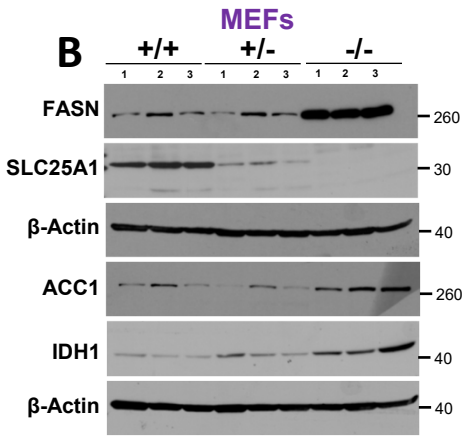
B
MEFs
+/+
+/-
-/-
FASN
SLC25A1
β-Actin
ACC1
IDH1
β-Actin
260
30
40
260
40
40

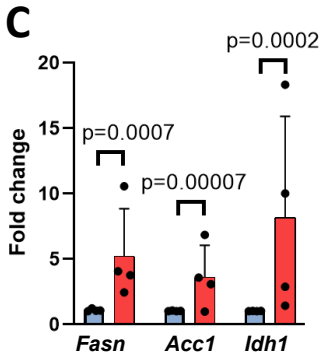
C
p=0.0002
p=0.0007
p=0.00007
Fold change
Fasn
Acc1
Idh1

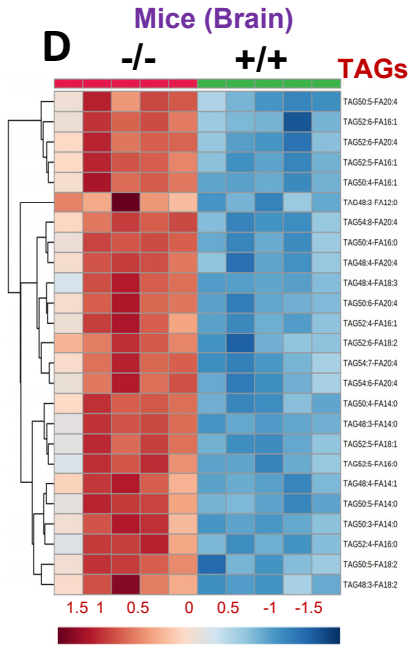
D
Mice (Brain)
-/-
+/+
TAGs

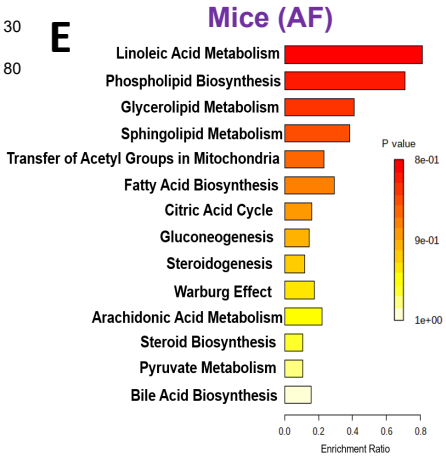
E
Mice (AF)
Linoleic Acid Metabolism
Phospholipid Biosynthesis
Glycerolipid Metabolism
Sphingolipid Metabolism
Transfer of Acetyl Groups in Mitochondria
Fatty Acid Biosynthesis
Citric Acid Cycle
Gluconeogenesis
Steroidogenesis
Warburg Effect
Arachidonic Acid Metabolism
Steroid Biosynthesis
Pyruvate Metabolism
Bile Acid Biosynthesis
P value
Enrichment Ratio

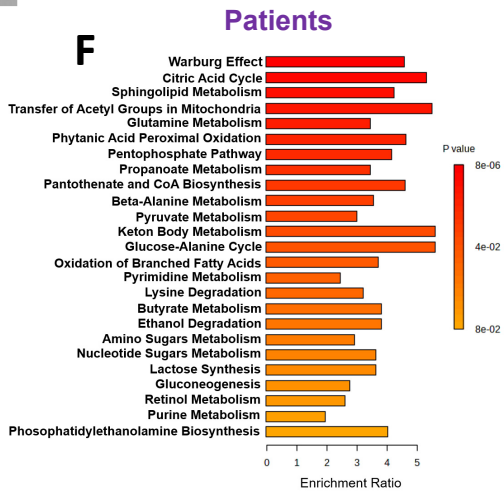
F
Patients
Warburg Effect
Citric Acid Cycle
Sphingolipid Metabolism
Transfer of Acetyl Groups in Mitochondria
Glutamine Metabolism
Phytanic Acid Peroximal Oxidation
Pentophosphate Pathway
Propanoate Metabolism
Pantothenate and CoA Biosynthesis
Beta-Alanine Metabolism
Pyruvate Metabolism
Keton Body Metabolism
Glucose-Alanine Cycle
Oxidation of Branched Fatty Acids
Pyrimidine Metabolism
Lysine Degradation
Butyrate Metabolism
Ethanol Degradation
Amino Sugars Metabolism
Nucleotide Sugars Metabolism
Lactose Synthesis
Gluconeogenesis
Retinol Metabolism
Purine Metabolism
Phosophatidylethanolamine Biosynthesis
P value
Enrichment Ratio

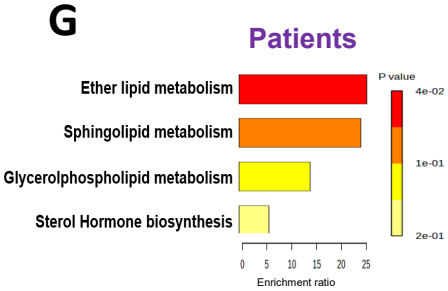
G
Patients
Ether lipid metabolism
Sphingolipid metabolism
Glycerolphospholipid metabolism
Sterol Hormone biosynthesis
P value
Enrichment ratio

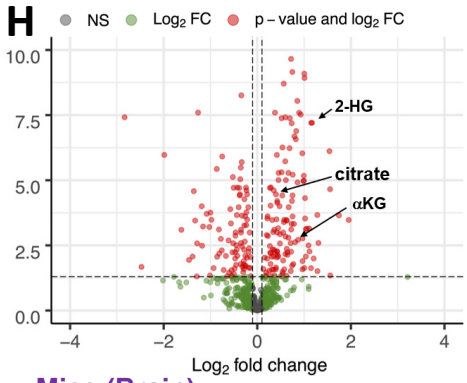
H
NS
Log2 FC
p – value and log2 FC
2-HG
citrate
αKG
−Log10 adjusted P
Log2 fold change

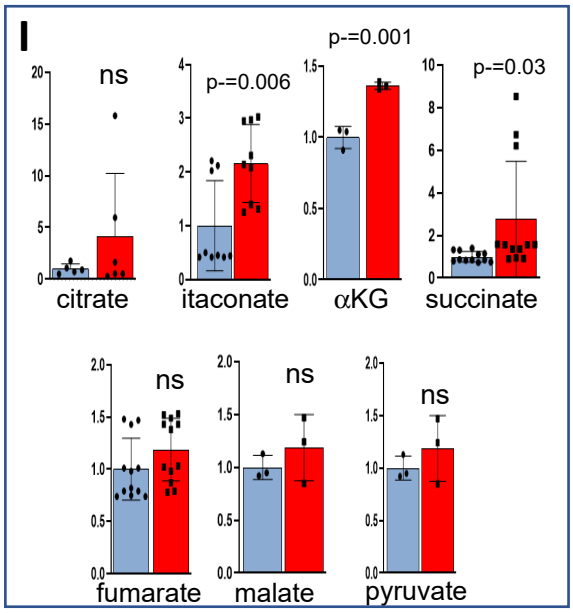
I
ns
p-=0.006
p-=0.001
p-=0.03
citrate
itaconate
αKG
succinate
ns
ns
ns
fumarate
malate
pyruvate

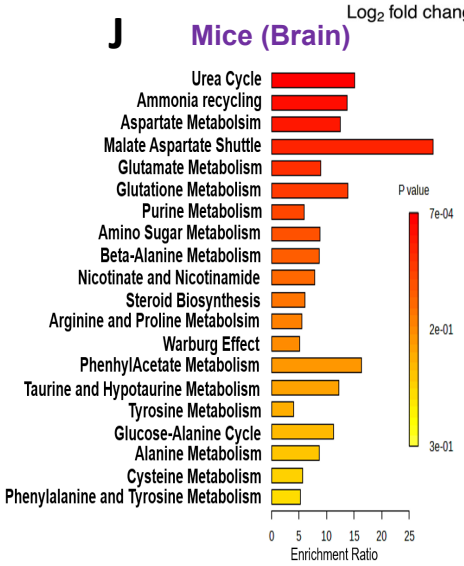
J
Mice (Brain)
Urea Cycle
Ammonia recycling
Aspartate Metabolsim
Malate Aspartate Shuttle
Glutamate Metabolism
Glutatione Metabolism
Purine Metabolism
Amino Sugar Metabolism
Beta-Alanine Metabolism
Nicotinate and Nicotinamide
Steroid Biosynthesis
Arginine and Proline Metabolsim
Warburg Effect
PhenhylAcetate Metabolism
Taurine and Hypotaurine Metabolism
Tyrosine Metabolism
Glucose-Alanine Cycle
Alanine Metabolism
Cysteine Metabolism
Phenylalanine and Tyrosine Metabolism
P value
Enrichment Ratio

Figure 4

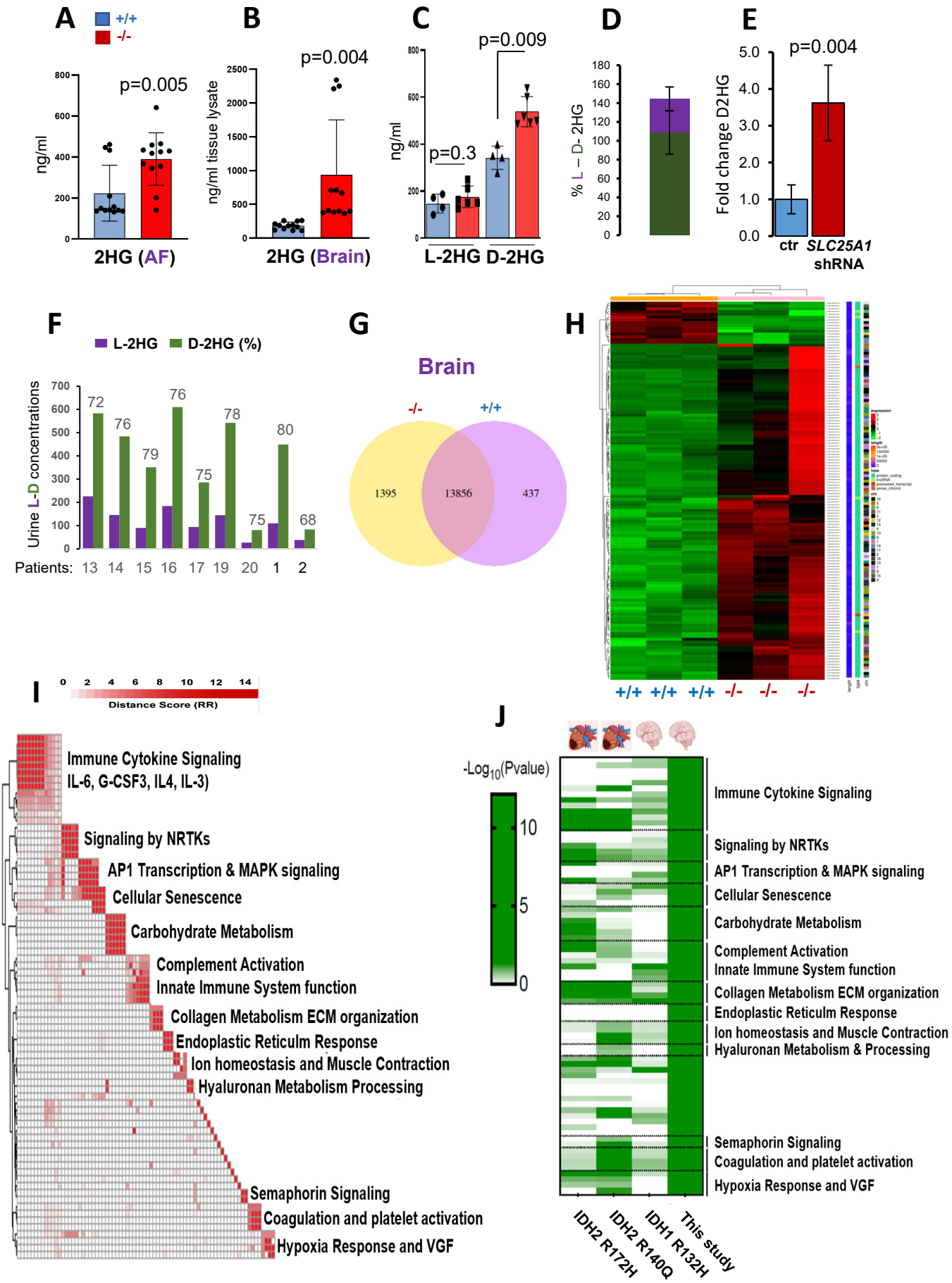
A
+/+
-/-
p=0.005
ng/ml
2HG (AF)
B
p=0.004
ng/ml tissue lysate
2HG (Brain)
C
p=0.009
p=0.3
ng/ml
L-2HG D-2HG
D
% L – D- 2HG
E
p=0.004
Fold change D2HG
ctr SLC25A1 shRNA
F
L-2HG D-2HG (%)
Urine L-D concentrations
Patients: 13 14 15 16 17 19 20 1 2
G
Brain
-/- +/+
1395 13856 437
H
+/+ +/+ +/+ -/- -/- -/-
I
Distance Score (RR)
Immune Cytokine Signaling
IL-6, G-CSF3, IL4, IL-3)
Signaling by NRTKs
AP1 Transcription & MAPK signaling
Cellular Senescence
Carbohydrate Metabolism
Complement Activation
Innate Immune System function
Collagen Metabolism ECM organization
Endoplastic Reticulm Response
Ion homeostasis and Muscle Contraction
Hyaluronan Metabolism Processing
Semaphorin Signaling
Coagulation and platelet activation
Hypoxia Response and VGF
J
-Log10(Pvalue)
Immune Cytokine Signaling
Signaling by NRTKs
AP1 Transcription & MAPK signaling
Cellular Senescence
Carbohydrate Metabolism
Complement Activation
Innate Immune System function
Collagen Metabolism ECM organization
Endoplastic Reticulm Response
Ion homeostasis and Muscle Contraction
Hyaluronan Metabolism & Processing
Semaphorin Signaling
Coagulation and platelet activation
Hypoxia Response and VGF
IDH2 R172H
IDH2 R140Q
IDH1 R132H
This study

Figure 5

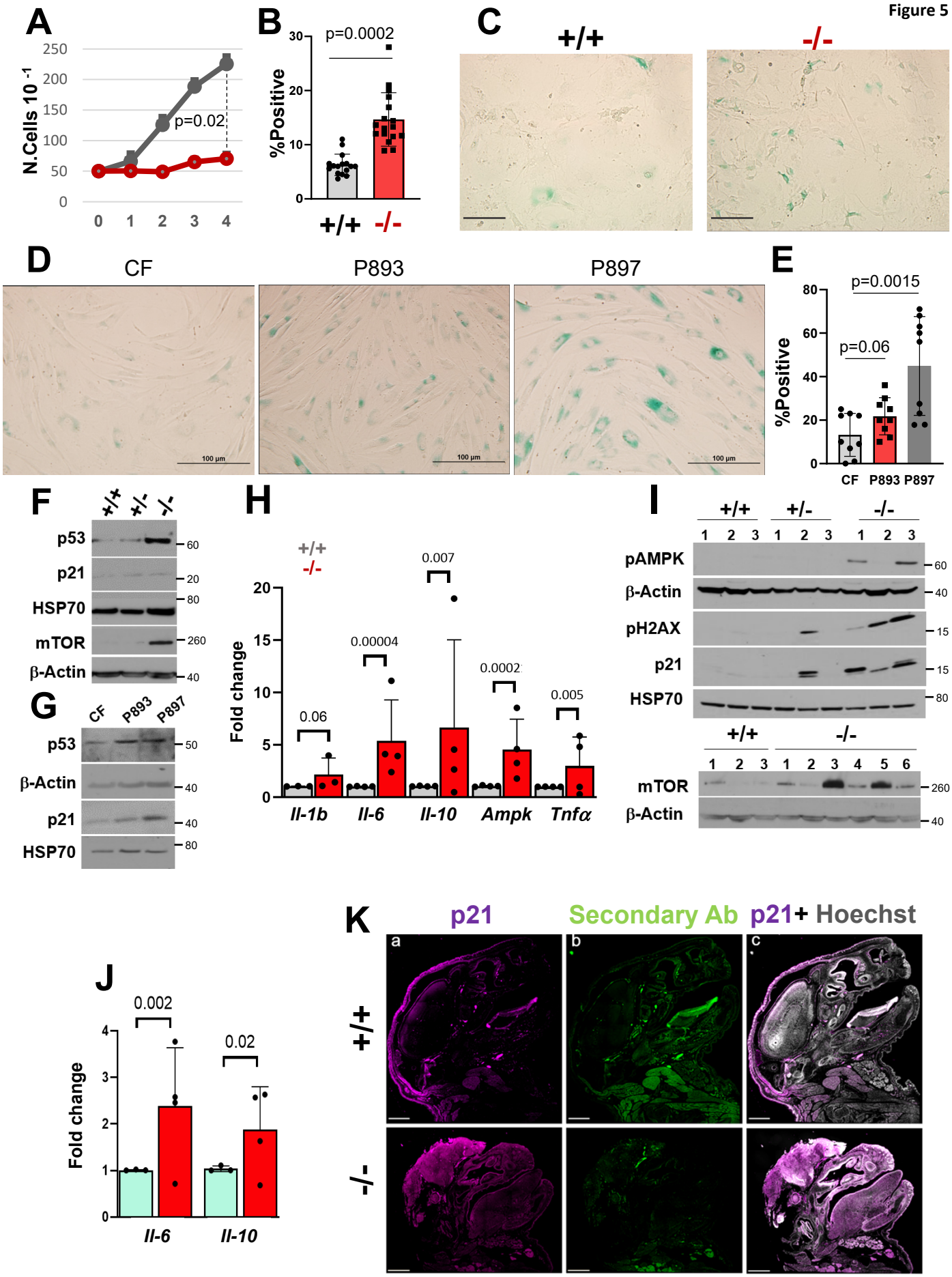
A
N.Cells 10 -1
250
200
150
100
50
0
0 1 2 3 4
p=0.02
B
%Positive
p=0.0002
+/+ -/-
C
+/+
-/-
D
CF
P893
P897
100 µm
E
%Positive
p=0.0015
p=0.06
CF P893 P897
F
+/+ +/- -/-
p53
p21
HSP70
mTOR
β-Actin
G
CF P893 P897
p53
β-Actin
p21
HSP70
H
+/+
-/-
Fold change
0.06
0.00004
0.007
0.0002
0.005
Il-1b Il-6 Il-10 Ampk Tnfα
I
+/+ +/- -/-
pAMPK
β-Actin
pH2AX
p21
HSP70
+/+ -/-
mTOR
β-Actin
J
Fold change
0.002
0.02
Il-6 Il-10
K
p21
Secondary Ab
p21+ Hoechst
+/+
-/-

Figure 6

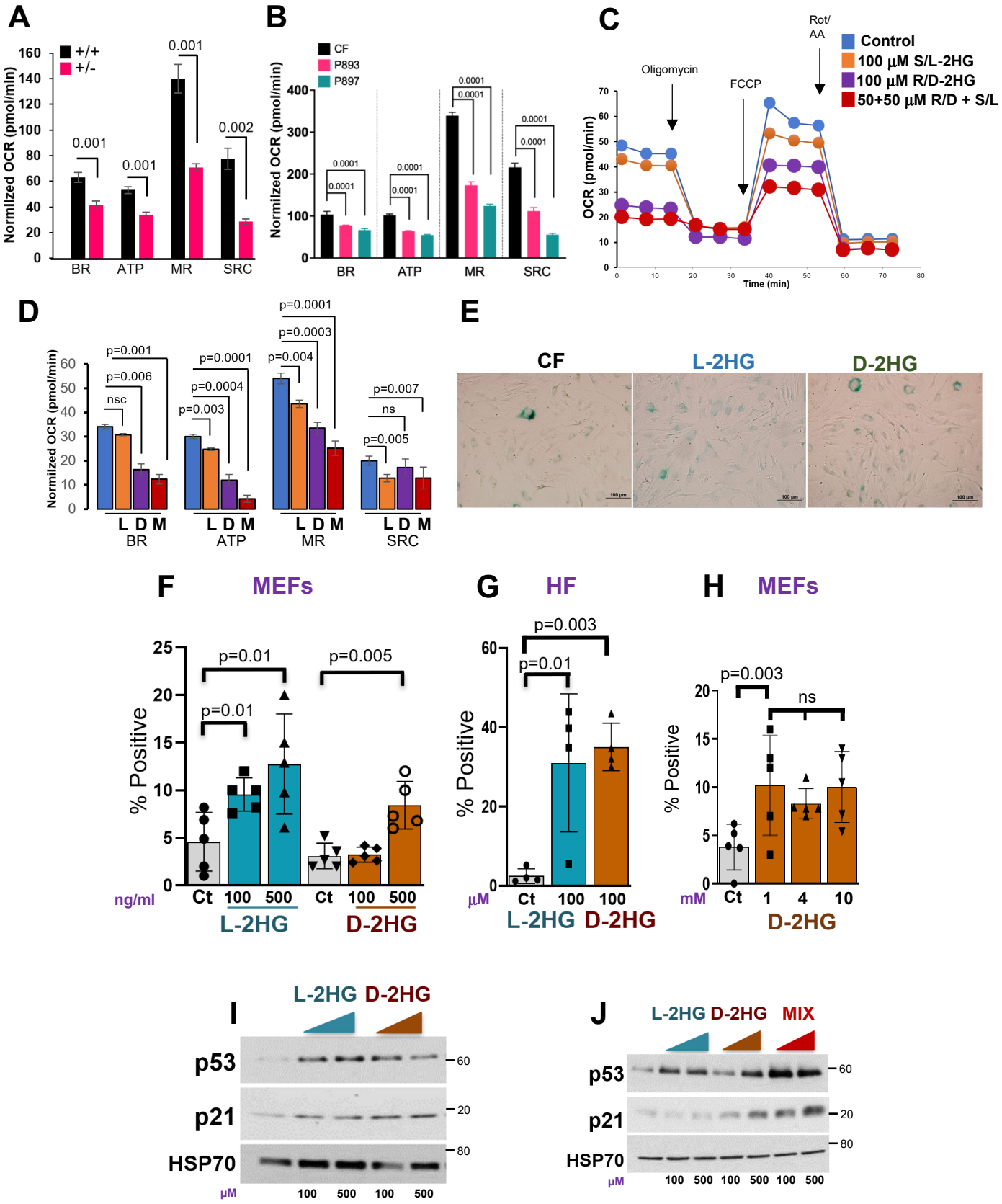
A
+/+
+/-
Normilzed OCR (pmol/min)
0.001
0.001
0.001
0.002
BR
ATP
MR
SRC
B
CF
P893
P897
Normilzed OCR (pmol/min)
0.0001
BR
ATP
MR
SRC
C
Rot/
AA
Control
100 µM S/L-2HG
100 µM R/D-2HG
50+50 µM R/D + S/L
Oligomycin
FCCP
OCR (pmol/min)
Time (min)
D
Normilzed OCR (pmol/min)
p=0.001
p=0.006
nsc
p=0.0001
p=0.0004
p=0.003
p=0.0001
p=0.0003
p=0.004
p=0.007
ns
p=0.005
L D M
BR
ATP
MR
SRC
E
CF
L-2HG
D-2HG
F
MEFs
% Positive
p=0.01
p=0.01
p=0.005
ng/ml
Ct
100
500
Ct
100
500
L-2HG
D-2HG
G
HF
% Positive
p=0.003
p=0.01
µM
Ct
100
100
L-2HG
D-2HG
H
MEFs
% Positive
p=0.003
ns
mM
Ct
1
4
10
D-2HG
I
L-2HG
D-2HG
p53
p21
HSP70
60
20
80
µM
100
500
100
500
J
L-2HG
D-2HG
MIX
p53
p21
HSP70
60
20
80
µM
100
500
100
500
100
500

Figure 7

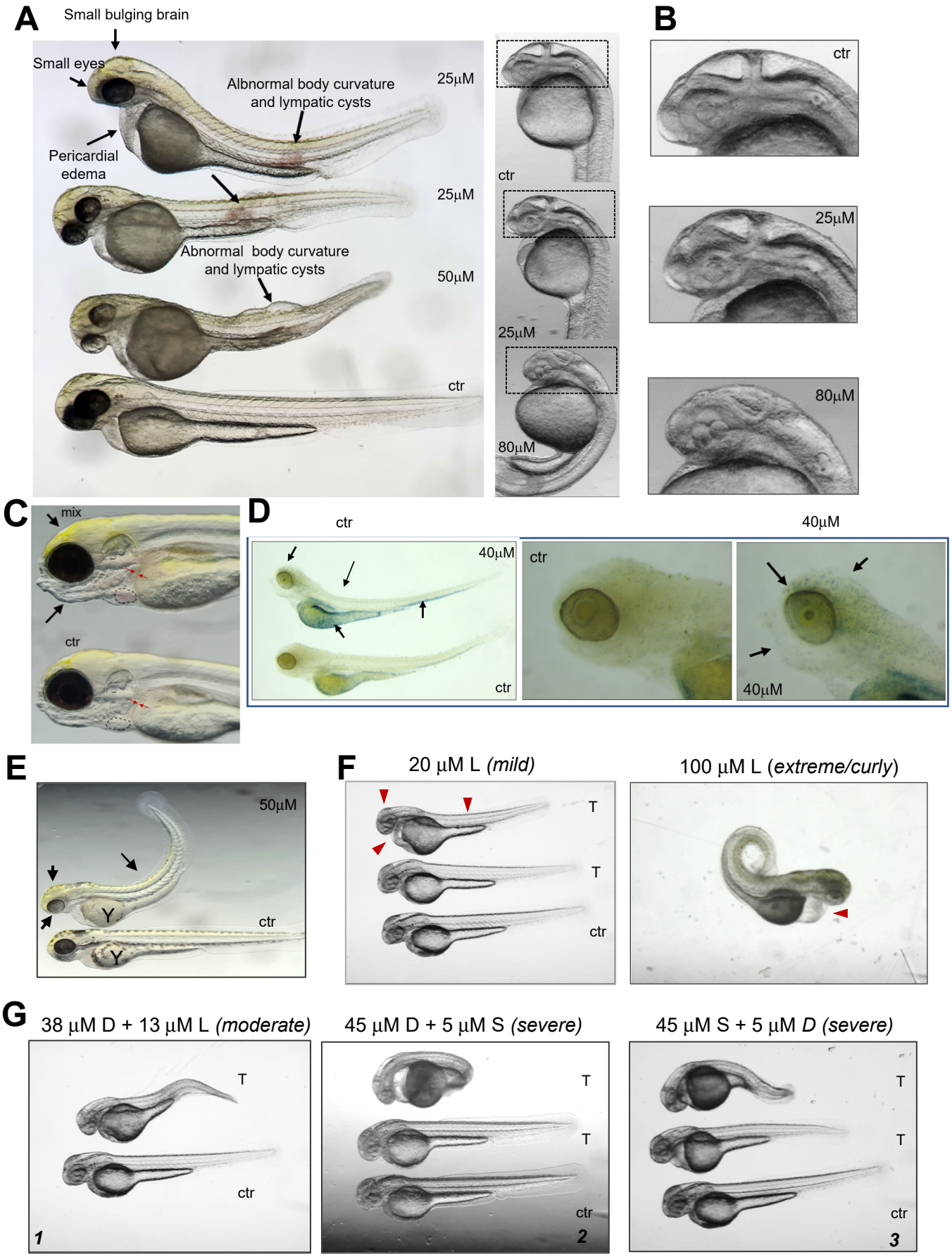
A
Small bulging brain
Small eyes
Albnormal body curvature
and lympatic cysts
25μM
Pericardial
edema
25μM
Abnormal body curvature
and lympatic cysts
50μM
ctr
ctr
25μM
80μM
B
ctr
25μM
80μM
C
mix
ctr
D
ctr
40μM
40μM
ctr
ctr
40μM
E
50μM
Y
ctr
Y
F
20 μM L (mild)
T
T
ctr
100 μM L (extreme/curly)
G
38 μM D + 13 μM L (moderate)
T
ctr
1
45 μM D + 5 μM S (severe)
T
T
ctr
2
45 μM S + 5 μM D (severe)
T
T
ctr
3

Figure 8

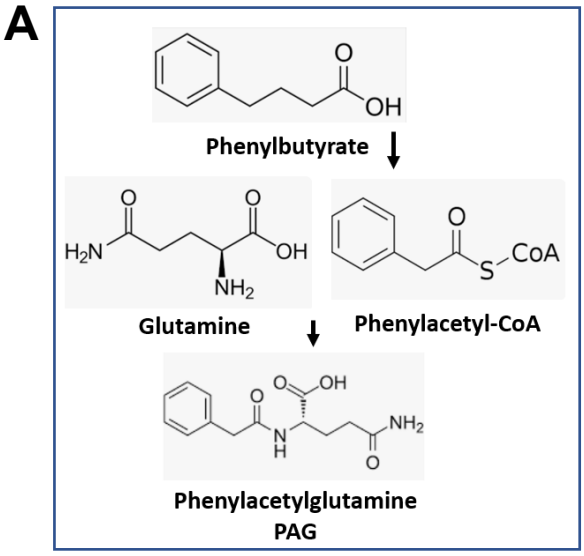

B

Objective Clinical Improvement under PB treatment (P897)
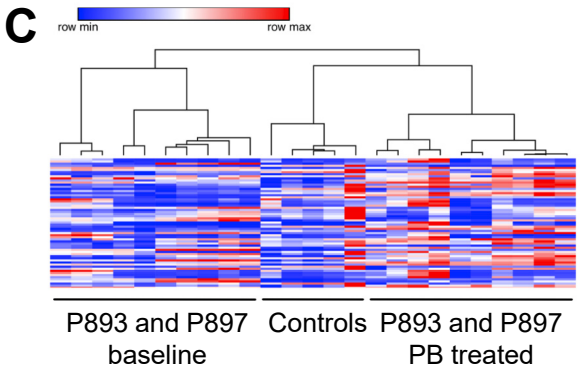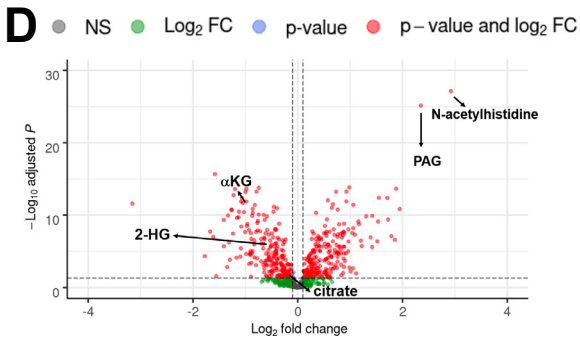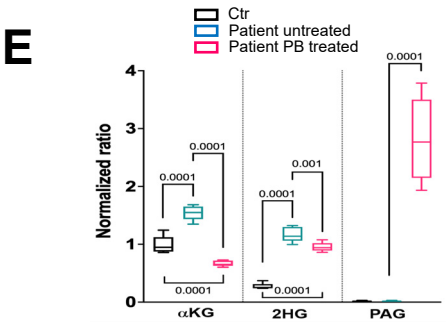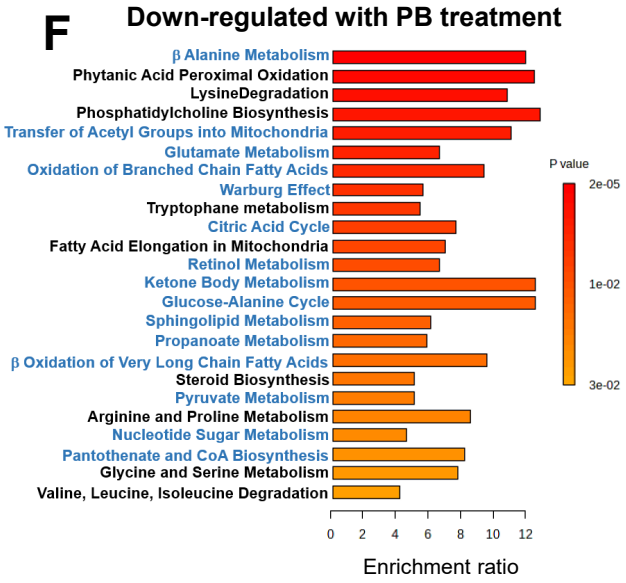
- Reduced ventilator dependency
- Increased awareness and QOL
- Reduced hospitalization